ORIGINAL ARTICLE

International Journal for Numerical Methods in Engineering

An Adaptive Eigenfunction Basis Strategy to Reduce Design Dimension in Topology Optimization

Clay Sanders[1]* | **Marc Bonnet PhD**[2]* | **Wilkins Aquino PhD**[2]†

[1]Department, Institution, City, State or Province, Postal Code, Country

[2]Department, Institution, City, State or Province, Postal Code, Country

Correspondence
Author One PhD, Department, Institution, City, State or Province, Postal Code, Country
Email: correspondingauthor@email.com

Present address
†Department, Institution, City, State or Province, Postal Code, Country

Funding information
Funder One, Funder One Department, Grant/Award Number: 123456, 123457 and 123458; Funder Two, Funder Two Department, Grant/Award Number: 123459

In this work, we present an adaptive eigenspace basis (AEB) strategy for design parameterization in topology optimization problems. Conventional representations of the density design variable with nodal or element-wise values suffer from large dimension and require costly filtering operations throughout the optimization procedure to ensure solution existence. We alternatively construct the density field as a linear combination of eigenfunctions, computed for an elliptic operator defined over the structural domain, and solve for the associated eigenfunction coefficients. Restriction to this finite-dimensional eigenspace drastically reduces the design dimension and imposes implicit regularization upon the solution, removing the need for auxiliary filtering operations and element-wise bound constraints. We furthermore develop a basis adaptation scheme, in which we iteratively recompute the eigenfunction basis to conform to the evolving solution field, enabling further dimension reduction and acceleration of the optimization process. The adapted eigenfunctions are specially-constructed to approximate piecewise constant fields, featuring localized variation at structural-void boundaries, and thus are adept at representing relevant design subspaces in low-dimension.

*Equally contributing authors.

We demonstrate the AEB method on topology optimization problems for static linear elasticity. We propose criteria for the selection of the basis dimension and demonstrate the use of basis-function selection as means for solution length scale control. We benchmark the performance of the AEB method against conventional TO implementations, obtaining comparable structural solutions with equivalent or decreased computational runtime while using design dimensions multiple orders of magnitude smaller than conventional parameterizations. The AEB strategy can easily be extended to TO problems for a variety of physics.

KEYWORDS
keyword 1, *keyword 2*, keyword 3, keyword 4, keyword 5, keyword 6, keyword 7

1 | INTRODUCTION

The aim of this paper is to formulate an effective design dimensionality-reduction scheme for density-based topology optimization. We propose representing the structural design, a spatially-varying “fictitious density" field that indicates distribution of material, using an adaptively-constructed basis of eigenfunctions defined over the structural domain. In this formulation, the typically high-dimensional design space may be represented in a much-lower dimensional form, with the sum of relatively few density modes able to parameterize the design. We find that the truncated eigenfunction basis representation may substitute conventional methods to regularize the design space, such as filtering operations applied to the underlying fictitious-density design field. Additionally, we propose a series of adaptive eigenfunction basis updates, allowing the design field to capture the evolving design in an increasingly compressed form. Structural solutions obtained with the AEB method, compared to conventional density-based methods, achieve comparable structural performance while enjoying benefits associated with a lower-dimensional optimization problem. We assert that our reduced-basis design approach offers attractive computational properties, associated with lower dimensional designs and the elimination of conventional filters, and would be amenable to topology optimization schemes for a variety of physics applications.

The conventional approach to the formulation of topology optimization problems is to represent the solution–the structural design–as a spatially-varying “fictitious-density" field, taking values in (0,1) and representing interpolation between two material extremes or solid and void. In discrete implementations, a vector of design variables corresponding to element or nodal density values parameterizes the design. Penalization of intermediate density values encourages the allocation of full-density in advantageous regions of the structural domain [1]. Filtering operations are necessarily employed to regularize the solution field and ensure solution existence, typically constructed as averaging kernel operations that preclude high-frequency or mesh-dependent variation in the solution [2] or heat-equation type PDE’s [3].

The expense of solving the topology optimization problem naturally increases as the computational domain grows in dimension; large or finely-discretized domains not only require expensive state-space (displacement) solutions, but

also feature design-space dimensions that grow in proportion to the state-space dimension. Strategies that reduce the dimension of the optimization problem, while incurring only slight effects upon solution quality, would offer attractive means to mitigate computational cost. In general, reduced-dimension representations of the design space may enable convergence in fewer iterations with improved stability. Second-order implementations involving the Hessian (or approximation of the Hessian), for instance, will have greatly reduced dimension and can enjoy improved convergence rates. In this work, we will address reduction of the design space dimension as means of improving the computational efficiency of solving the topology optimization problem.

Design space dimensionality reduction in topology optimization, though not widely studied, has previously been performed through various adaptive schemes. Guest et al. proposed an adaptive formulation of a “Heaviside projection method", which used a material indicator function to turn on and off design variables, in an adaptive manner, inside moving Heaviside radial projection regions [4]. The approach adaptively reduced the design space dimension by isolating the design variables subject to changes in value, principally those along the structural domain boundary. However, computational savings are limited by the non-smooth nature of the Heaviside projection and the use of genetic algorithms, which can incur heavy cost through numerous objective function evaluations.

In a similar vein, adaptive mesh refinement in topology optimization is a useful strategy to refine the evolving structural-void boundary and thereby allocate computational expense efficiently. In these strategies, goal-oriented error estimators can indicate regions of high solution or geometry interpolation error, identifying these regions as candidates for mesh refinement, while regions with low error may be coarsened without impact to solution error [5, 6]. Multiple field solutions, in which separate meshes model the state and design fields, further reduce the dimension design represented by the adaptive meshes [7]. These methods, however, still require filtering operations to avoid development of mesh-dependent solutions and checkerboard patterns and retain high-dimensional design spaces for highly-refined structural domains.

We propose the use of a reduced eigenfunction basis, computed for an elliptic operator defined over the domain, to represent the density-based design. We use an adaptive reduced eigenspace basis approach, as has been recently formulated in parameter identification optimization problems for steady-state elastodynamics [8, 9] and electromagnetics [10]. In this approach, we confine the solution to the span of a basis of eigenfunctions of an elliptic operator defined over the structural domain. Our design variables become the coefficients associated with the eigenfunctions, enabling a significant reduction in the dimensionality of the design space. The truncated low-frequency basis also serves as a form of implicit regularization upon the design field, preventing the evolution of mesh-dependent, oscillating solutions; thus, the filtering operations typically required to control for mesh-dependence and checkerboarding become unnecessary. As we explain in the sequel, we construct the eigenfunction design representation to ensure the density solution respects (0,1) bounds while also preventing solution convergence to large-magnitude basis coefficients.

Furthermore, we propose an adaptive scheme to adjust the eigenfunction basis to the developing density-field solution. As proposed in [9] and [10], eigenfunctions may be computed in an adaptive manner so that their spatial variation is concentrated in regions of the solution with large spatial density gradients, where the solution is likely to change. In a series of optimization problems, we compute a design solution then compute a new basis of eigenfunctions, using the current solution to construct a new elliptic operator for the eigenvalue problem. As the eigenfunctions of these operators are constructed to conform to the developing solution and represent piecewise constant solutions in low-dimension, we can pursue further reduction of the design dimension. Previous studies have noted that the adapted elliptic operators used to compute the bases coincide with the gradient of the total-variation regularization functional [9], often used in image-processing and de-noising applications to identify and preserve sharp interfaces. The eigenfunctions of the adapted elliptic operators inherit these properties, as topology optimization can be inter-

preted as the discovery and definition of optimal structural-void interfaces, and thus represent a particularly useful candidate basis to construct topology optimization solutions.

The proposed method has several benefits that make it an attractive alternative to conventional density-based methods. We chiefly observe a significant reduction of the necessary design space dimension; in our 2D implementation, we reduce the design variable dimension by 1-2 orders of magnitude with little loss in the quality of the structural design. The truncated basis eliminates the need for filtering operations throughout the optimization procedure, thus eliminating the computational costs associated with filtering the solution and gradients each iteration. The adaptive scheme enables further reduction of the design dimension through multiple optimization passes and emphasizes refinement of the structural-void boundary. We note that restricting designs to any finite-dimensional subspace naturally constrains potential solutions; thus, by restricting designs to the eigenspace basis, we may not necessarily achieve solutions with improved performance (i.e. lower objective function evaluations) than solutions using a traditional element-wise parameterization. While not explored here, our adaptive scheme could be paired with existing mesh adaptivity strategies, as has been explored in previous AEI studies [10], to refine the mesh and concentrate solution resolution near parameter discontinuities.

The rest of the paper is organized as follows. First, we present the formulation of the topology optimization problems of interest. In Section 3, we formulate the eigenfunction basis design problem, presenting the associated eigenvalue problems to construct the bases and the supplementary projection and regularization strategies. We present optimality criteria in Section **??**. We present, in Section 4, the adaptive strategy used to construct the series of eigenfunction bases and demonstrate, in Section 4.3, the accuracy and efficiency with which the adapted bases may represent a target structure. We provide criteria to select the basis dimension in Section 4.4 and implementation details in Section **??**. Finally, we demonstrate the merits of the approach in several examples of static displacement minimization design problems.

2 | TOPOLOGY OPTIMIZATION PROBLEM

2.1 | Forward Problem

We first introduce the topology optimization problem used to demonstrate our reduced-basis design strategy: the design of linear-elastic structures with minimal displacement under static loading, subject to a volume fraction constraint. We represent the elastostatic boundary value problem governing the displacement response $\boldsymbol{u}$ of a body Ω, under traction τ and in the absence of body forces, in weak form: find $\boldsymbol{u} \in \mathcal{W}$ such that

$$a(\boldsymbol{u}, \boldsymbol{w}) = l(\boldsymbol{w}), \forall w \in \mathcal{W},$$

where $\mathcal{W} := \{\boldsymbol{w} : \boldsymbol{w} \in H^1(\Omega), \boldsymbol{w} = \boldsymbol{0} \text{ on } \Gamma_D\}$. We define

$$a(\boldsymbol{u}, \boldsymbol{w}) := \int_\Omega \boldsymbol{\epsilon}[\boldsymbol{u}] : \mathbb{C} : \boldsymbol{\epsilon}[\boldsymbol{w}] \, d\Omega$$
$$l(\boldsymbol{w}) := \int_{\Gamma_N} \boldsymbol{w} \cdot \tau \, d\Gamma_N$$

where Γ_N is the Neumann boundary, Γ_D is the Dirichlet boundary, with $\Gamma_N \cup \Gamma_D = \partial\Omega$, $\Gamma_N \cap \Gamma_D = \varnothing$, $\boldsymbol{\epsilon}[\boldsymbol{u}] = \frac{1}{2}(\nabla \boldsymbol{u} + \nabla \boldsymbol{u}^T)$ is the linearized small-strain tensor, and $\mathbb{C} = \mathbb{C}(\boldsymbol{x})$ is a positive, bounded, spatially-varying fourth-order constitutive tensor, where $\boldsymbol{x} \in \Omega$. We assume linear-elastic, isotropic behavior, and thus may parameterize $\mathbb{C}(\boldsymbol{x}) = \mathbb{C}(G(\boldsymbol{x}), \kappa(\boldsymbol{x}))$,

with $G(\boldsymbol{x})$ and $\kappa(\boldsymbol{x})$ spatially-varying, real shear and bulk moduli.

We introduce a finite-dimensional approximation of $\boldsymbol{u}$ with a finite element discretization $\boldsymbol{u}_h = [N]\boldsymbol{d}$, with $[N]$ the matrix of global shape functions and $\boldsymbol{d} \in \mathbb{R}^{n_d}$ nodal displacement values. Substitution of this approximation for trial functions, and similarly for test functions, in Eq. 1 yields

$$[K]\boldsymbol{d} = \boldsymbol{f}$$

where $[K]$ is the stiffness matrix, $\boldsymbol{f}$ is the forcing vector. We use $[]$ notation to represent matrix quantities and boldface for vector quantities. We use the following definitions for the construction of $[K]$ and $\boldsymbol{f}$

$$[K] := \sum_e \int_{\Omega_e} [B]_e^T [D]_e [B]_e \, d\Omega_e$$
$$[D]_e := G_e[D_G] + \kappa_e[D_b]$$
$$\boldsymbol{f} := \sum_{e \in \Gamma_N} \int_{\Gamma_{Ne}} [N]_e^T \boldsymbol{\tau} \, d\Gamma_e$$

in which $\sum_e$ represents the assembly operator over elements, Ω_e is the element domain, $[B]_e$ is the matrix of derivatives of element shape functions $[N]_e$, $[D]_e$ is the elasticity matrix is composed of shear component $[D_G]$ and bulk component $[D_\kappa]$ with element-specific elastic constants G_e and κ_e, and Γ_{Ne} is the portion of an element boundary on the Neumann boundary.

2.2 | Structural Objective

Structural performance is evaluated with objective $\mathcal{D}(\boldsymbol{d})$, a functional of displacements satisfying differentiability requirements for gradient based methods. In this work, we select $\mathcal{D}(\boldsymbol{d})$ as a discrete approximation of the squared L^2-norm of displacements over a measured subdomain $\Omega_m \subseteq \Omega$

$$\mathcal{D}(\boldsymbol{d}) = \frac{1}{2}\boldsymbol{d}^T [Q]\boldsymbol{d}$$

where $[Q]$ is a Boolean measurement matrix, with ones in the diagonal entries corresponding to the targeted degrees of freedom and zeros elsewhere. We note other common objectives, such as static compliance (e.g [11]) may be substituted.

2.3 | Density Design Representation

In a density-based TO formulation, a “fictitious density" field $\beta(\boldsymbol{x})$ describes the spatial distribution of the material within the domain, indicating distinct material phases or void and solid. An element-wise constant parameterization $\boldsymbol{\beta} \in \mathbb{R}^{n_e}$, with n_e the number of elements, takes values in $[0, 1]$ and interpolates the element elastic properties κ_e and G_e between distinct sets of material properties $\{\kappa_0, G_0\}$ and $\{\kappa_1, G_1\}$. Density parameterizations employ penalization, in conjunction with a constraint on the structural volume, to discourage intermediate values of the design variable [1]. We adopt the Solid Isotropic Microstructure with Penalization (SIMP) model [11], which applies an exponential penalization p to the densities within the evaluation of the material models. Furthermore, additional density-filtering [2] and Heaviside-projection [12] operations must be performed upon $\boldsymbol{\beta}$ to ensure mesh-independence and 0-1 valued

designs; the “analysis density" field $h(\boldsymbol{\beta})$ produced by these operations is input in the material evaluation. We thus represent the SIMP model

$$\kappa_e = \kappa(h_e; p) = \kappa_0 + \Delta\kappa\ h_e^p$$
$$G_e = G(h_e; p) = G_0 + \Delta G\ h_e^p$$

where $p = 3$, $\Delta G := (G_1 - G_0)$, $\Delta\kappa := (\kappa_1 - \kappa_0)$, and h_e is the element $h(\boldsymbol{\beta})$ value. We may represent the system in Eq. 4 as an operator on $\boldsymbol{\beta}$ and $\boldsymbol{d}$

$$c(\boldsymbol{\beta}, \boldsymbol{d}) := [K(\boldsymbol{\beta})]\boldsymbol{d} - \boldsymbol{f} = \mathbf{0}$$

2.4 | Topology Optimization Problem

In this work, we will use a reduced-space formulation for the topology optimization problem, in which we represent the state variable $\boldsymbol{d}$ as an implicit function of control $\boldsymbol{\beta}$. It may be shown that for a given value $\boldsymbol{\beta}^*$, the discretized PDE system in Eq. 4 admits a unique value $\boldsymbol{d}^*$, satisfying $c(\boldsymbol{\beta}^*, \boldsymbol{d}^*) = \mathbf{0}$. Namely, the derivative of $c(\boldsymbol{\beta}^*, \boldsymbol{d}^*)$ with respect to $\boldsymbol{d}$ (which we denote $c'_{\boldsymbol{d}}$) has a continuous, bounded inverse, implying well-posedness of the elastostatic BVP. By the implicit function theorem, $\boldsymbol{d}$ may be represented as an implicit function $\boldsymbol{d} = \boldsymbol{d}(\boldsymbol{\beta})$ [13]. Thus, we define a reduced objective, a function of only the design, as

$$\tilde{\mathcal{D}}(\boldsymbol{\beta}) := \mathcal{D}(\boldsymbol{d}(\boldsymbol{\beta})).$$

We pose the optimization problem:

$$\boldsymbol{\beta}^* = \arg\min_{\boldsymbol{\beta}\in\mathbb{R}^{ne}} \tilde{\mathcal{D}}(\boldsymbol{\beta})$$
$$\text{subject to: } 0 \le \beta_e \le 1$$
$$V_C = \frac{1}{V_\Omega}\sum_e \int_{\Omega_e} h_e\, d\Omega_e - v_{max} \le 0$$

Eq. 14 represents the volume fraction constraint upon the analysis density field, with V_Ω the domain volume and v_{max} the maximum volume fraction.

2.5 | Derivative Evaluation

In this section, we use an adjoint-based formulation to derive the gradient of the objective with respect to the densities. Adjoint-based formulations to compute derivatives are widely-used, due to their computational efficiency, and can be found, for instance, in [13]. Under the implicit function theorem, $\boldsymbol{d}$ is continuously differentiable with respect to $\boldsymbol{\beta}$. We express the directional derivative of $\tilde{\mathcal{D}}$ with respect to $\boldsymbol{\beta}$, in direction $\boldsymbol{p}$, through application of the chain rule

$$\langle \tilde{\mathcal{D}}'_{\boldsymbol{\beta}}, \boldsymbol{p}\rangle = \langle \mathcal{D}'_{\boldsymbol{d}}, \boldsymbol{d}'_{\boldsymbol{\beta}}\boldsymbol{c}\rangle + \langle \mathcal{D}'_{\boldsymbol{\beta}}, \boldsymbol{p}\rangle$$
$$= \langle \boldsymbol{d}'^{T}_{\boldsymbol{\beta}}\, \mathcal{D}'_{\boldsymbol{d}} + \mathcal{D}'_{\boldsymbol{\beta}}, \boldsymbol{p}\rangle$$

where $\langle S'_{\boldsymbol{\beta}}, \boldsymbol{p} \rangle$ represents the Gâteaux derivative of a functional S with respect to $\boldsymbol{\beta}$ in direction $\boldsymbol{p}$ and $\boldsymbol{d}'^{T}_{\boldsymbol{\beta}}$ is formed using the definition of an adjoint operator [13]. To eliminate sensitivity $\boldsymbol{d}'^{T}_{\boldsymbol{\beta}}$, we first define the adjoint variable $\boldsymbol{v} := \boldsymbol{v}(\boldsymbol{\beta}) \in \mathbb{R}^{n_d}$ which solves the adjoint problem

$$\boldsymbol{c}'^{T}_{\boldsymbol{d}} \boldsymbol{v} = -\mathcal{D}'_{\boldsymbol{d}}$$

We equivalently express the adjoint problem in discrete form as

$$[K]\boldsymbol{v} = -[Q]\boldsymbol{d}.$$

Additionally, taking the derivative of Eq. 10 with respect to $\boldsymbol{\beta}$ yields

$$\boldsymbol{c}'_{\boldsymbol{d}} \boldsymbol{d}'_{\boldsymbol{\beta}} = -\boldsymbol{c}'_{\boldsymbol{\beta}}$$

Using Eq. 17 and Eq. 19 in Eq. 16, and noting $\mathcal{D}'_{\boldsymbol{\beta}} = \mathbf{0}$, we express the full derivative (expressed with respect to β_e) as

$$\tilde{\mathcal{D}}'_{\beta_e} = \boldsymbol{c}'^{T}_{\beta_e} \boldsymbol{v} = \left((\boldsymbol{d}_e)^T [K']_e \boldsymbol{v}_e \right) (h'_{e,\boldsymbol{\beta}})$$

where $[K']_e$ is the derivative of the element stiffness matrix with respect to h_e, $\boldsymbol{d}_e$ and $\boldsymbol{v}_e$ are the forward and adjoint variable values corresponding to a given element, and $h'_{e,\boldsymbol{\beta}}$ is the derivative of h_e with respect to the $\boldsymbol{\beta}$ field. We evaluate

$$[K']_e = \int_{\Omega_e} [B]_e^T \left[G'_{h_e} [D_G] + \kappa'_{h_e} [D_\kappa] \right] [B]_e \, d\Omega_e$$
$$\text{with } G'_{h_e} = p \Delta G h_e^{p-1}, \kappa'_{h_e} = p \Delta \kappa \, h_e^{p-1}.$$

3 | EIGENSPACE BASIS DESIGN FORMULATION

Conventional density-based TO methods formulate the design problem of binary placement of material using the continuous $\boldsymbol{\beta}$ variable spatially-varying throughout the domain; in most discretized settings, as presented in Section 2, this quantity is represented with piecewise-constant element values. The design variable thus suffers from high-dimensionality, as the design variable will possess dimension on the order of the number of degrees of freedom used in the discretization. Conventional parameterizations require regularization–through filtering or homogenization operations–to ensure existence of solutions, to impose minimum lengthscales, and to avoid mesh-dependence or checkerboarding numerical issues [2]. Fine discretization may improve resolution of the structural topology, at the cost of increasing design dimension, but in a regularized setting should not change the qualitative form of the structural solution. Structural designs are ultimately characterized by multi-element, rather than element-to-element, features, a concept not leveraged by element-wise or nodal parameterizations.

We propose a new, reduced-basis approximation of the density field to address issues of solution dimensionality and regularity. Beginning in a continuous setting, we construct $\boldsymbol{\beta}(\boldsymbol{x})$ as a linear combination of eigenfunction basis

(EB) members $\psi_i(\boldsymbol{x}) \in H^1(\Omega)$, with coefficients $b_i \in \mathbb{R}$

$$\beta(\boldsymbol{x}) := \sum_{i=1}^{\ell} b_i \psi_i(\boldsymbol{x})$$

Let this truncated set of eigenfunctions have dimension $\ell < \infty$ and the vector of coefficients be $\boldsymbol{b} \in \mathbb{R}^{\ell}$. We select ψ_i from the eigenfunctions of an elliptic operator defined over the design domain. The eigenfunctions solve the generalized eigenvalue boundary-value problem (EVP), with homogeneous Neumann boundary conditions,

$$\begin{cases} -\nabla \cdot (\mu(\boldsymbol{x}) \nabla \psi_i(\boldsymbol{x})) = \lambda_i \psi_i(\boldsymbol{x}) & \text{in } \Omega \\ \nabla \psi_i(\boldsymbol{x}) \cdot \boldsymbol{n} = 0 & \text{on } \partial\Omega \end{cases}$$

where $\mu(\boldsymbol{x})$ is a spatially-varying tensor of coefficients ($\mu(\boldsymbol{x}) = [I]$ corresponds to the Laplacian operator) and $\lambda_1 \leq \lambda_2 \leq \ldots \leq \lambda_\ell$ are associated eigenvalues. Note, we define Neumann-eigenfunctions, rather than Dirichlet-eigenfunctions used in previous EB parameter inversion formulations [8], because we have no a priori knowledge of the solution field at the boundary $\partial\Omega$.

We express the weak-form of Eq. 23, and introduce a finite-dimensional approximation of the trial eigenfunctions $\psi_{ih} = [N_1]\phi_i$ and test functions, where $[N_1]$ are global scalar-valued shape functions and ϕ_i the eigenfunction nodal-values, yielding the discretized generalized eigenvalue problem

$$[K_1^{(i)}]\phi_i = \lambda_i [M_1]\phi_i$$

for $i = 1 \ldots \ell$. Here, we define

$$[K_1^{(i)}] := \sum_e \int_{\Omega_e} [B_1]_e^T [\mu]_e [B_1]_e d\Omega_e$$
$$[M_1] := \sum_e \int_{\Omega_e} [N_1]_e^T [N_1]_e d\Omega_e.$$

where $[B_1]_e$ is the matrix of derivatives for element scalar shape functions $[N_1]_e$, and $[\mu]_e$ is the coefficient matrix for the element. We obtain the element-wise $\beta_e(\boldsymbol{b})$ as the linear combination of nodal-valued eigenfunctions evaluated at element centroids $\bar{\boldsymbol{x}}_e$

$$\beta_e(\boldsymbol{b}) = \sum_{i=1}^{\ell} [N_1(\bar{\boldsymbol{x}}_e)]_e \phi_{ie} b_i$$

where ϕ_{ie} are the element nodal values for ϕ_i. We henceforth will use $\boldsymbol{\beta}$ as the vector of β_e and $[\Phi] = [\phi_1, \phi_2, \ldots, \phi_\ell]$ as the matrix of eigenfunctions.

By using the ℓ eigenfunctions associated with the lowest ℓ eigenvalues as a basis, we restrict our solution to reside in the a finite-dimensional subspace spanned by the column-space of $[\Phi]$ and, in effect, embed regularization into the design space. As we will develop further in Section 4, adaptive construction of the coefficient field $[\mu]_e$ will produce eigenfunctions that can represent piecewise-constant solution fields with efficiency. We next describe operations performed upon the EB-expanded design variable to ensure convergence to binary solutions and to finite basis coefficients.

3.1 | Logistic Projection

In conventional density-based methods, regularization methods such as filtering operations ensure the existence and mesh-independence of solutions, though produce undesirable intermediate density values [2]. High-contrast solution quality is regained through “multiple-field strategies", where filtered densities are projected upon nonlinear Heaviside function approximations to produce the “analysis density" that is finally input into the penalized material model [14, 15]. In our formulation, the truncated EB restricts the design space, thereby inducing regularization of the solution as would a filter operation. We do, however, utilize a Heaviside-approximator to map the $\boldsymbol{\beta}$ field, which may take any real value, to near 0 or near 1 values, both ensuring ensuring inputs into the SIMP model are in (0,1) and encouraging high-contrast solution quality. Accordingly, we adopt an element-wise nonlinear logistic projection function

$$h(\beta_e;\zeta) := \frac{1}{1+e^{-\zeta(\beta_e)}}$$

parameterized by a slope constant $\zeta > 0$. Let $\boldsymbol{h}$ represent the vector of $h(\beta_e)$. The logistic projection, shown in Figure 18 for various ζ values, is bounded between 0 and 1, ensuring all $\boldsymbol{h}$ satisfy SIMP input bounds. Negative densities are projected closer to zero and positive densities closer to one, with the slope ζ controlling the severity of the projection about the origin.

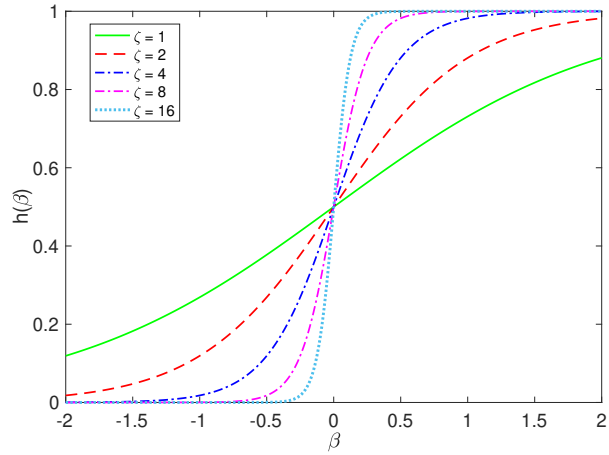

FIGURE 1 Logistic projection function, for various slope parameter values.

3.2 | Double-Well Potential Regularization

The eigenfunction representation of the solution will restrict the solution to possess the displayed lengthscale characteristics of the basis functions. By projecting $\boldsymbol{\beta}$ onto the logistic function, we further ensure that inputs into the SIMP model satisfy (0,1) bounds. However, in minimum-displacement topology optimization, under material penalization and volume constraints, optimal solutions encourage placement of full material or complete elimination of material (i.e. $h(\beta_e) = 0$ or $h(\beta_e) = 1$) to maximize the structural stiffness for a given volume [2]. For a finite ζ, analysis densities $h(\beta_e) = 1$ or $h(\beta_e) = 0$ may be achieved only with $\beta_e \to \pm\infty$, thus requiring coefficients $\boldsymbol{b} \to \pm\infty$, representing a non-

existent solution. Bound constraints cannot be placed upon $\boldsymbol{b}$, as the ideal magnitude for coefficients is not known a priori. We instead propose a double well potential (DWP) functional term be added to the objective to control the magnitude of the $\boldsymbol{\beta}$ field

$$W(\boldsymbol{b}) = \frac{1}{V_\Omega} \sum_e \int_{\Omega_e} (\beta_e(\boldsymbol{b}) - 1)^2 (\beta_e(\boldsymbol{b}) + 1)^2 d\Omega_e$$

A weighting scalar α is applied to the DWP term in the objective function. The DWP integrand, a quartic-polynomial plotted in Fig. 2, is strictly positive, except at values $\beta_e = \pm 1$. The DWP regularization offers the attractive benefit of clustering the $\boldsymbol{\beta}$ field near ± 1, penalizing densities both in $(-1, 1)$, thus providing a control on transitions between solid and void, as well those with large magnitude, preventing excessively large b_i values. We can exploit the bimodal quality of $\boldsymbol{\beta}$ solutions regularized by the DWP term in adaptation and compression of the eigenfunction basis, as we will describe in Section 4. Our use of the DWP term for regularization of the basis coefficients is similar to the study in [16], which uses a DWP penalty term to relax 0-1 constraints in a phase-field topology optimization formulation. Interplay of the logistic projection function and the weighting applied to the DWP term controls the convergence of the solution to optimal topology with nearly binary analysis density values.

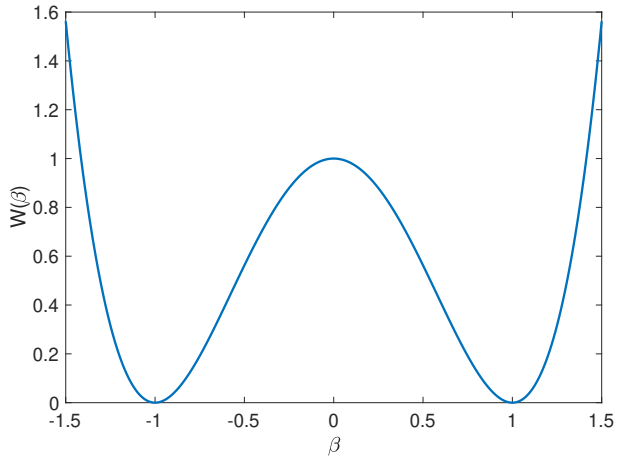

FIGURE 2 Double-well potential objective term versus input pseudo-density.

3.3 | Eigenspace Basis Design Problem

We may restate the topology optimization problem, now seeking the optimal basis coefficients. Let the objective for the EB design problem, including the DWP term, be

$$\mathcal{J}(\boldsymbol{b}) := \mathcal{D}(\boldsymbol{d}) + \alpha W(\boldsymbol{b}),$$

where α is a scalar coefficient. We use similar arguments as in Section 2.4 to pose a reduced-space formulation. With the density field now parameterized by the eigenbasis, we redefine, from Eq. 10, $c(\boldsymbol{b}, \boldsymbol{d}) := c(\boldsymbol{\beta}(\boldsymbol{b}), \boldsymbol{d})$. The system

$c(\boldsymbol{b}, \boldsymbol{d}) = 0$ admits a unique value $\boldsymbol{d}$ for a value $\boldsymbol{b}$; by the implicit function theorem, $\boldsymbol{d}$ may be represented as an implicit function $\boldsymbol{d} = \boldsymbol{d}(\boldsymbol{b})$. The reduced objective may be defined

$$\tilde{\mathcal{J}}(\boldsymbol{b}) := \mathcal{D}(\boldsymbol{d}(\boldsymbol{b})) + \alpha W(\boldsymbol{b}),$$

and we may pose the optimization problem

$$\begin{aligned} \boldsymbol{b}^* &= \arg\min_{\boldsymbol{b}\in\mathbb{R}^\ell} \tilde{\mathcal{J}}(\boldsymbol{b}) \\ \text{subject to: } V_C &= \frac{1}{V_\Omega} \sum_e \int_{\Omega_e} h(\beta_e(\boldsymbol{b}))\, d\Omega_e - v_{max} \leq 0. \end{aligned}$$

3.4 | Derivative Evaluation

We may borrow from the derivation in Section 2.5 to express the gradient of the reduced AEB objective with respect to basis coefficients. The directional derivative of the reduced objective $\tilde{\mathcal{J}}$, in direction $\boldsymbol{p}$, may again be expressed through application of the chain rule

$$\langle \tilde{\mathcal{J}}'_{\boldsymbol{b}}, \boldsymbol{p} \rangle = \langle \boldsymbol{d}'^T_{\boldsymbol{b}}\, \mathcal{J}'_{\boldsymbol{d}} + \mathcal{J}'_{\boldsymbol{b}}, \boldsymbol{p} \rangle$$

We find, through substitution of the adjoint solution $\boldsymbol{v}$ from Eq. 18, and using Eq. 19,

$$\tilde{\mathcal{J}}'_{\boldsymbol{b}} = c'^T_{\boldsymbol{b}} \boldsymbol{v} + \mathcal{J}'_{\boldsymbol{b}}.$$

We may express the discrete evaluation of these derivatives, with respect to individual basis coefficient components b_i, as

$$\begin{aligned} \mathcal{J}'_{b_i} &= \alpha W'_{b_i} = \alpha \frac{1}{V_\Omega} \sum_e \int_{\Omega_e} 2(\beta_e - 1)(\beta_e + 1)^2 + 2(\beta_e + 1)(\beta_e - 1)^2 \phi_{ie}\, d\Omega_e \\ c'^T_{b_i} \boldsymbol{v} &= \sum_e \left((\boldsymbol{d}_e)^T [K'_e] \boldsymbol{v}_e \right) (h'_{e,\beta_e}) \phi_{ie} \end{aligned}$$

We express h'_{e,β_e}, the derivative of the logistic function, as

$$h'_{e,\beta_e} = \frac{e^{-\zeta\beta_e}}{\left(1 + e^{-\zeta\beta_e}\right)^2}$$

and ϕ_{ie} is the element value for ϕ_i. We also evaluate the gradient of the volume inequality constraint as

$$V'_{C,b_i} = \frac{1}{V_\Omega} \sum_e \int_{\Omega_e} h'_{e,\beta_e} \phi_{ie}\, d\Omega_e$$

4 | ADAPTIVE EIGENSPACE BASIS CONSTRUCTION

Reduction of the design space dimension may be enhanced, and acceleration of the overall optimization process achieved, through a multi-step basis-update strategy. In this section, we present an adapted eigenspace basis (AEB) strategy to enrich the EB with which the design solution is represented, based upon the strategy presented in [10]. Through multiple optimization passes, the EB is reconstructed using information from the current solution to capture global structural features in low-dimensional form and concentrate variation near shifting structural-void interfaces. The proposed basis adaptation will permit consistent reduction in the dimension of design variables throughout the optimization process, as few, specialized eigenfunctions may be used to express the structural form.

4.1 | Adapted Eigenvalue Problem Construction

Prior to each "pass", representing a single optimization solution, a new EB is computed from an EVP whose elliptic operator is constructed using the solution from the previous pass. The new EVPs are seeded with unique spatially-varying coefficient fields $[\mu]$ within their second-order differential operators that increasingly emphasize regions where the fictitious-density spatial gradient is large.

4.1.1 | Pass 1

In the first pass, we utilize a basis of eigenfunctions of the Laplacian eigenvalue problem, setting the coefficient matrix in Eq. 23 as $[\mu^{(1)}]_e = [I]$, where $[I]$ is the identity matrix. We obtain $[\Phi^{(1)}]$ from Eq. 24, and then solve the optimization problem (Eq. 32) to determine $\boldsymbol{b}^{(1)}$ and density fields $\boldsymbol{\beta}^{(1)}$ and $\boldsymbol{h}^{(1)}$.

4.1.2 | Pass 2

In the second pass, we construct a new elliptic operator whose eigenfunctions will exhibit localized features in regions with large spatial density gradients. We first interpolate $\boldsymbol{\beta}^{(1)}$ onto the nodal basis, obtaining nodal values $\boldsymbol{\beta}_N^{(1)}$. We then define a field of element-wise isotropic coefficients as

$$[\mu^{(2)}]_e := \frac{1}{\max\left(|\nabla\boldsymbol{\beta}_{Ne}^{(1)}|, \epsilon\right)}[I]$$

where $\boldsymbol{\beta}_{Ne}^{(1)}$ are values of $\boldsymbol{\beta}_N^{(1)}$ for an element and $\epsilon = 1e-6$ prevents the denominator from disappearing. We evaluate the gradient term $|\nabla\boldsymbol{\beta}^{(1)}| = |[B_1]e\boldsymbol{\beta}_{Ne}^{(1)}|$.

Eigenfunctions of the EVP with $[\mu^{(2)}]_e$, which is is inversely-proportional to the density gradient norm, will tend to exhibit high-frequency, localized spatial variation in regions with low μ values and low-frequency (near-constant) values in regions with high μ values [8]. We solve the EVP (Eq. 24) for $[\Phi^{(2)}]$ and then solve the design problem (Eq. 32) to determine $\boldsymbol{b}^{(2)}$ and density fields $\boldsymbol{\beta}^{(2)}$ and $\boldsymbol{h}^{(2)}$.

4.1.3 | Pass 3

In the third pass, we increase the order of the gradient term in the denominator of the coefficient field, further emphasizing the density gradient. We define

$$[\mu^{(3)}]_e = \frac{1}{\max\left(|\nabla \beta_{Ne}^{(2)}|^2, \epsilon\right)}[I]$$

where we evaluate the gradient term as in Eq. 40. We solve the EVP (Eq. 24) for $[\Phi^{(3)}]$. We then determine the coefficient solution $b^{(3)}$ by solving the optimization problem and compute the associated density fields $\beta^{(3)}$ and $h^{(3)}$.

4.1.4 | Pass 4

In the final optimization pass, we construct spatially-varying, anisotropic coefficients for the EVP, increasing the order of the gradient denominator term in the direction of the density gradient, normal to the structural-void interface. Using rotation matrix $[P]$, we define a coordinate transformation from base coordinates $\boldsymbol{x} = \{x_1, x_2\}$ to an orthogonal set of coordinates $\boldsymbol{X} = \{X_1, X_2\}$, for which X_1 is colinear with the density gradient [10]. The rotation matrix is constructed

$$[P]_e := \frac{1}{|\nabla \beta_{Ne}^{(3)}|}\begin{bmatrix} \frac{\partial \beta_{Ne}^{(3)}}{\partial x_1} & -\frac{\partial \beta_{Ne}^{(3)}}{\partial x_2} \\ \frac{\partial \beta_{Ne}^{(3)}}{\partial x_2} & \frac{\partial \beta_{Ne}^{(3)}}{\partial x_1} \end{bmatrix}$$

The coordinate transformation is illustrated in Fig. 3. We then construct the coefficient field

$$[\mu^{(4)}]_e := \frac{1}{\max(|\nabla \beta_{Ne}^{(3)}|, \epsilon)}[P]_e[C]_e[P]_e^{-1}$$

$$[C]_e := \begin{bmatrix} \frac{1}{\max(|\nabla \beta_{Ne}^{(3)}|^2, \epsilon)} & 0 \\ 0 & 1 \end{bmatrix}$$

where $[C]$ is the anisotropic tensor emphasizing the X_1 normal direction in the rotated coordinates. In summary, these coefficient fields are defined with increasing powers of the fictitious-density gradient norm in the denominator, which cause eigenfunctions to exhibit increasing localization in transition regions near structural-void discontinuities.

4.2 | Justification for Adaptive Eigenfunction Decomposition

The proposed adapted basis strategy has been shown to possess several characteristics that lend to its application in topology optimization. The initial Laplacian eigenfunction basis qualitatively resembles sinusoidal functions with different spatial frequencies; thus, it has the flexibility to represent arbitrary design patterns, but is not necessarily well-suited for approximation of discontinuous, piecewise constant fields. Due to the well-known “Gibb’s phenomenon", oscillatory “ringing" occurs near discontinuities in piecewise constant fields approximated by a Fourier series expansion of sinusoidal bases [8]. The global oscillatory quality of the eigenfunctions will require a greater number of basis members to represent a given topology with nuanced, local features. In contrast, the adapted basis functions are ideal for representing piecewise constant fields, as they have concentrated variation near transition regions between

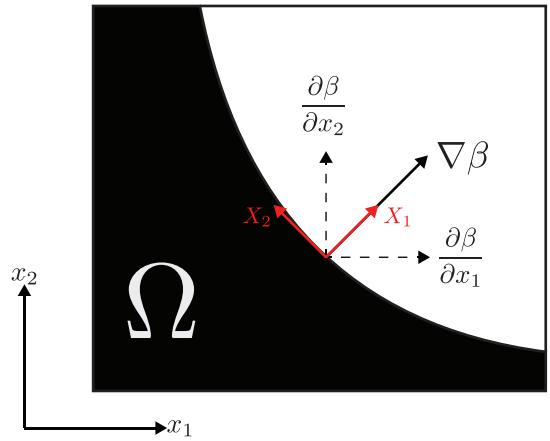

FIGURE 3 Rotation to coordinates aligned with density gradient.

void and solid and near-constant values elsewhere. As noted by [8, 9], decomposition of the parameter field upon the adapted eigenspace basis represents an analogous operation to total-variation regularization. The smoothed total-variation operator $R_{TV}(\beta)$ is defined

$$R_{TV}(\beta) := \frac{1}{2}\int_\Omega \sqrt{(|\nabla\beta|^2 + \epsilon^2}\, d\Omega$$

where ϵ is a small constant. The second-order operators defined in the adapted eigenvalue problems (with coefficient fields constructed as in Eq. 40) bare similarity to the gradient of the smoothed T_V operator

$$\begin{aligned}\nabla R_{TV} &\approx \int_\Omega -\nabla \cdot \left(\frac{1}{\sqrt{|\nabla\beta|^2 + \epsilon^2}} \nabla\beta \right) d\Omega \\ &\approx \int_\Omega -\nabla \cdot (\mu^{(2)}(\boldsymbol{x}) \nabla\beta)\, d\Omega\end{aligned}$$

Total-variation regularization penalizes high-frequency variation, rather than sharp discontinuities. The T_V operator has been shown to preserve or capture sharp transitions in solution fields for image processing, de-noising, and parameter identification inverse-problem applications [17]. The proposed eigenfunctions behave similarly, able to capture contiguous constant regions of material and void while attenuating intra-region and high spatial frequency variation. **NOTE: Here I could cite Grote's work from WAVES (but it is unpublished?), that it may be shown that a piecewise constant field containing k distinct, continuous regions may be approximated by $k+1$ distinct Neumann eigenfunctions, etc.** The adapted eigenfunctions permit efficient representation of structural topologies, as density design parameterizations approximate sharp discontinuities between regions of void and full material. Increasing the power of the gradient norm in $[\mu^{(3)}]$, and further orienting anisotropic weights orthogonal to structural-void boundaries in $[\mu^{(4)}]$, intensifies the edge-defining qualities of the eigenfunctions.

Importantly, our choice of the double-well potential term helps ensure that the developing density field can exploit the edge-defining properties of the adapted eigenfunctions. By penalizing large and small magnitude β values, the DWP term helps cluster β in neighborhoods near the two minima of the DWP functional, at $\beta = \pm 1$. As a result, β is steered towards piecewise constant values, ideally suited for low-dimensional representation by the adapted

eigenfunctions.

4.3 | Adapted Basis Representation Accuracy

A principal strength of the AEB is its ability to represent piecewise constant density-fields in low-dimensional form. In the following study, we demonstrate these qualities by computing the projection of a target pattern $\boldsymbol{\beta}^*$ upon bases constructed from eigenfunctions computed with the different spatial-coefficient seeds. The target design, shown in Figure 4, is a 2×1 MBB beam design containing $140 \times 70 = 9800$ elements; black-values have $\beta_e^* = 1$ and white values, $\beta_e^* = 0$.

FIGURE 4 Target MBB design for representation study.

We compute eigenbases corresponding to each of the EVP schemes proposed in Section 4, using a nodal-projection of the target solution $\boldsymbol{\beta}_N^*$ to construct the coefficient fields $[\mu^{(i)}]_e$. In each case, we compute the first 400 eigenfunctions. We then compute the L^2-projections of the target solution onto the four bases with increasing dimension, where the L^2-projection of the target field upon an eigenbasis (of dimension j) is computed as the solution of the least-squares minimization problem

$$\boldsymbol{b}_j^* = \underset{\boldsymbol{b} \in \mathbb{R}^j}{\arg\min} \frac{1}{2} \|\boldsymbol{\beta}_N^* - \boldsymbol{\beta}_j^{(i)}\|_{L^2(\Omega)}^2 = \frac{1}{2} \left\| [N_1]\boldsymbol{\beta}_N^* - [N_1][\Phi_j]\boldsymbol{b}_j \right\|^2$$

whose solution $\boldsymbol{b}_j$ solves

$$[M_\Phi]\boldsymbol{b}_j = [\Phi_j]^T [M_1]\boldsymbol{\beta}_N^*,$$

where $[M_\Phi] := [\Phi]^T [M_1][\Phi]$ is the eigenfunction mass-matrix. We can compute the relative L^2 residual $\boldsymbol{\epsilon}_j^{(i)}$ between $\boldsymbol{\beta}_N^*$ and $\boldsymbol{\beta}_j^{(i)}$ as

$$\boldsymbol{\epsilon}_j^{(i)} := \frac{\|\boldsymbol{\beta}_N^* - \boldsymbol{\beta}_j^{(i)}\|_{M_1}}{\|\boldsymbol{\beta}_N^*\|_{M_1}}.$$

where we define a discrete L^2-norm of the nodal-density field $\boldsymbol{\beta}_N$ as

$$\|\boldsymbol{\beta}_N\|_{M_1} := \sqrt{\boldsymbol{\beta}_N^T [M_1]\boldsymbol{\beta}_N}.$$

Results indicate the exceptional ability of the AEB to adapt to a given domain with discontinuous constant fields. Figure 5 shows resulting density fields produced from the L^2-projections of the target design upon the adapted eigenspace bases with dimensions $\ell = \{8, 32, 200\}$. The relative errors between the target and L^2-projected pseudo-

densities (Fig. 6 for various basis dimensions depict the improved accuracy and efficiency with which the AEB match the target structure. Projections using the initial Laplacian basis functions slowly approximate the target field; eventually, a few-hundred eigenfunctions reasonably capture the structural features with L^2-error reaching 20.1% for $\ell = 400$. With each adaptive eigenfunction construction, projection accuracy improves– projection errors are 6.7%, 5.8%, and 5.3% for passes 2-4 for bases of dimension 400– as does the dimensional efficiency with which low errors are achieved. In Pass 3 and 4, eigenbases of dimension 16 achieve error 6.7% and 4.9%, respectively, with error actually increasing slightly for the larger-dimensional bases in Pass 4, as these EF's may represent numerical error artifacts rather than distinct, linearly-independent modes. We note that solving Eq. 49 for an element-wise target solution naturally introduces numerical error during the projection onto the nodal basis, which would preclude our implementation from reaching very low projection error.

Inspection of the EF's, as sampled in Figure 7, shows the edge-defining qualities of the adapted eigenfunctions. The initial Laplacian EF's assume sinusoidal quality, with low-index EF's representing basic sinusoidal patterns and higher-index EF's, the superposition of complicated harmonics. The second-pass AEB functions begin capturing the global structural form in lower index eigenfunctions and concentrating localized variation in high-index EF's. In the third and fourth passes, the global structural patterns are captured with just the lowest-index EF's; by index 8, for instance, we see EF's representing specific, highly-localized regions of variation in the pseudo-density field.

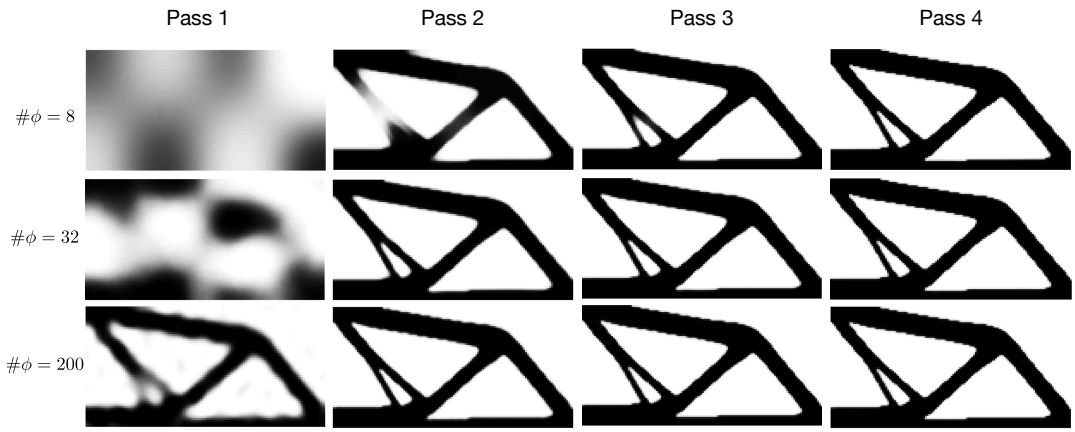

FIGURE 5 L^2 projections of target structure onto eigenfunction bases of increasing dimension.

4.4 | Criteria for Eigenspace Basis Selection

The AEB design parameterization enables substantial design space reduction; selection of the basis dimension, however, is a key factor in the quality of the structural solution. Basis truncation involves the inevitable trade-off between restriction of the subspace available for exploration and favorable computational benefits obtained with reduced design dimensionality.

Relatively ad-hoc criteria for basis dimension have been proposed for existing adaptive eigenspace bases in inverse problem settings. In frequency-domain inversion approaches, the spatial resolution of the detected parameter features changes with measurement frequency; thus parameter inversion approaches have selected basis dimension

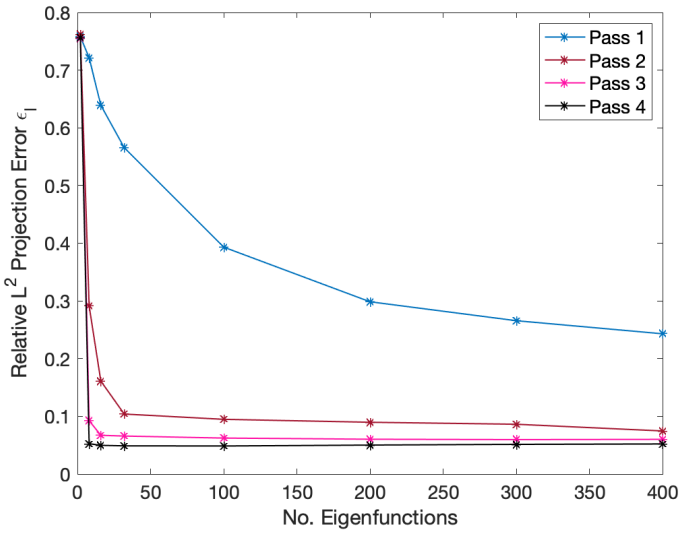

FIGURE 6 Relative L^2-error of pseudo-density projections to target field for bases of various dimensions.

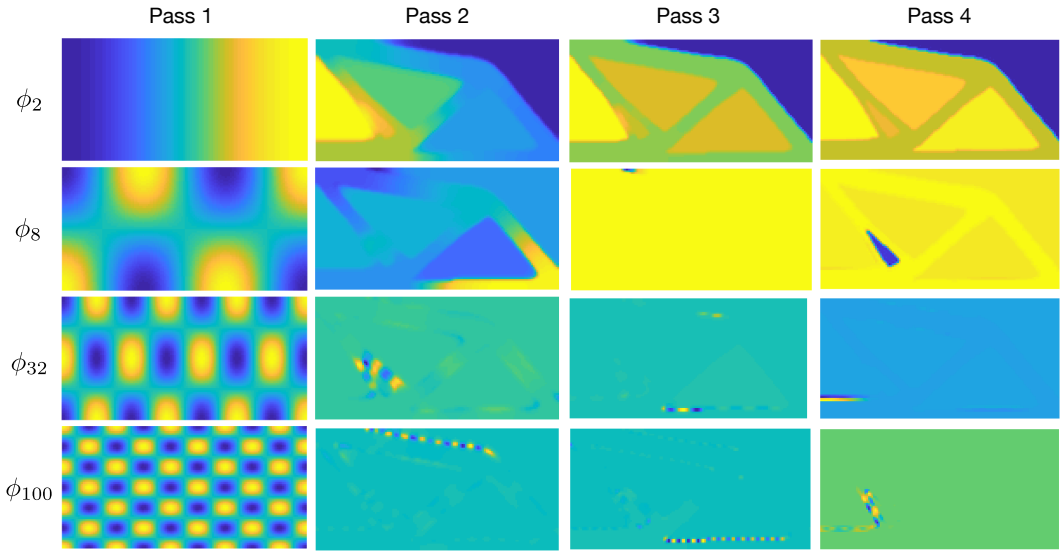

FIGURE 7 Example eigenfunctions computed from the four successive eigenvalue problems.

with respect to the wavelength of measurement frequency [10] or have gradually increased basis dimension using frequency-stepping algorithms [8]. However, we observe that geometric qualities of Laplacian eigenfunctions–namely the wavelength of spatial variation–may be inferred from the concurrently-calculated eigenvalue spectrum and used to convey length scale controls in TO design. Feature length scale and structural complexity are thus implicitly deter-

mined by the subset of eigenfunctions chosen, particularly during the first optimization pass. In the adaptive passes, basis selection can be further controlled to decrease dimension while ensuring minimal perturbation from the solution of one pass and the initial guess in the next pass. In this section, we will define criteria to select the initial and adapted eigenbasis dimensions.

4.4.1 | Initial Pass

We propose selecting the first basis dimension with respect to the spatial frequency characteristics of the Laplacian eigenfunctions. The set of Laplacian eigenfunctions will possess sinusoidal character, so we may interpret truncation of the basis as the filtering of specific frequency content from the spatial solution, as is performed in conventional filter operations. First, we note the Rayleigh quotient associated with a given eigenfunction ψ_i (i.e. its eigenvalue λ_i), corresponds to the squared inverse of the mean spatial wavelength w_i of the respective eigenfunction.

$$\lambda_i = \frac{\int_\Omega |\nabla \psi_i|^2 \, d\Omega}{\int_\Omega \psi_i^2 \, d\Omega}$$

$$k_i = 2\pi \sqrt{\frac{1}{\lambda_i}}$$

Eigenfunctions associated with large eigenvalues are characterized by high-frequency oscillation; truncation of the eigenfunction basis restrains this short wavelength spatial variation and will implicitly control solution minimum length scale. Alternatively, the maximum length scale of structural members can be controlled through additional truncation of low-frequency components, removing large-wavelength variation from the solution field. We calculate the corresponding mean spatial wavelength associated with a given eigenfunction and compare values to maximum and minimum wavelength thresholds ($\{k_{max}, k_{min}\}$) to cutoff eigenfunctions from either end of the eigenfunction spectrum. Wavelength thresholds may be selected to correspond approximately to the minimum (or maximum) feature width d desired in the structural design, (e.g. we may use $d_{min} \approx 1/2k_{min}$).

We may tie this basis truncation to the effect of PDE-based filters. Existing PDE-based filter operations (e.g. [3] compute a filtered density field by solving a heat-type equation, with β acting as “forcing" inputs, and essentially attenuate high-frequency content from the solution in order to ensure solution existence. Lazarov et. al showed that PDE-based filters may be constructed for both low-pass and band-pass scenarios, enabling implicit control of small (and large) length scales appearing in structural solutions [18]. We can view the truncation of our Laplacian eigenbasis as a straightforward filtering operation which explicitly removes frequency content from the solution eigenspectrum, with the added benefits of being performed only once in the optimization problem and trivially applied to non-rectangular domains.

We note truncation with respect to a specified wavelength/frequency may not explicitly remove all frequency content outside specified frequency thresholds–as eigenfunctions may contain a combination of different spectral components centered at a mean frequency. This extraneous frequency content tends to have low spectral power, however, contributing little to the spatial characteristics of a given eigenfunction.

We can briefly demonstrate eigenfunction spectral qualities by computing the spatial Fast Fourier Transform (SFFT) of eigenfunctions and plotting their amplitude spectra; eigenfunctions of a sample rectangular domain, and the respective SFFT, are shown in Fig. 8. We add circles with radii equal to the dominant frequency predicted by the corresponding eigenvalue and see coincidence of the predicted dominant frequencies with the radial distribution of spectral power. Low-index eigenfunctions contain concentrated spectral content exactly at the predicted frequency,

while high-index eigenfunctions contain more distributed frequency content, nevertheless concentrated radially at the predicted frequency. Thus, comparing these principal wavelengths to a threshold length scale $\{k_{min}, k_{max}\}$ can provide criteria to restrain the spatial variation represented within an eigenbasis.

4.4.2 | Subsequent Adaptive Passes

In selecting the adapted basis members in subsequent passes, we have several objectives: 1) to ensure that our initial guess on the new eigenfunction basis be close to our previous solution; 2) utilize eigenfunctions that contribute most to the current design; and 3) to maintain or decrease the dimension of our basis with each successive pass. High-index eigenfunctions are typically characterized by highly-localized, sparse spatial variation that may contribute little to representing, or improving, the solution. Accordingly, basis-truncation is still be used to restrain high-frequency spatial variation. Continued compression of the basis is also desirable as it may enable the use of advantageous computational (e.g. second-order) methods. Taking these objectives in mind, we propose an L^2-error criteria to select the AEB dimension.

First, we evaluate the relative L^2-residuals between the current solution, represented on the old basis, and its projections onto expanding subsets of the new basis. Let $[\Phi_j^{(i)}]$ represent the new adapted basis of dimension j, where eigenfunctions are ordered by their corresponding eigenvalues. We may evaluate the following relative L^2-error

$$\epsilon_j = \frac{\|\boldsymbol{\beta}^{(i-1)} - [\Phi_j^{(i)}]\boldsymbol{b}_{0,j}^{(i)}\|_{M_1}}{\|\boldsymbol{\beta}^{(i-1)}\|_{M_1}}.$$

Here, $\boldsymbol{b}_{0,j}^{(i)}$ are the coefficients for the L^2 projection of the previous $\boldsymbol{\beta}^{(i-1)}$ upon the new basis of dimension j, as computed with Eq. 49. Making use of the orthogonality of the eigenfunctions, we note that the L^2-projection of $\boldsymbol{\beta}^{(i-1)}$ upon any single eigenfunction is orthogonal to the remaining eigenfunction subspace. Lower-index eigenfunctions are generally, but not necessarily, associated with larger L^2-projection components. Thus, we may reorder the eigenfunction basis with respect to the independent, relative decrease in L^2-error associated with each eigenfunction to prioritize eigenfunctions that contribute most to the current solution. We may define the marginal L^2 error decrease, associated with eigenfunction ϕ_j, as

$$\hat{\epsilon}_j := (\epsilon_j - \epsilon_{j-1})$$

and reorder the eigenfunctions according to $\hat{\epsilon}_j$. In Figure 9, we show the L^2-error decrease versus eigenfunction index for the eigenvalue-ordered and error-ordered eigenfunctions presented in the representation study in Section 4.3 . We may finally define the relative projection error decrease, due to a given eigenfunction, as

$$c_j = \frac{\hat{\epsilon}_j}{\sum_{i=1}^{j-1} \hat{\epsilon}_i}$$

The L^2 error typically decreases rapidly within the few adapted eigenfunctions and afterwards decays slowly for additional eigenfunction contributions, thus c_j will monotonically decrease. We may truncate the reordered eigenfunction basis with respect to a tolerance on c_j, indicating that the L^2 error is negligibly decreasing with increased basis dimension. We summarize the AEB algorithm for solving the topology optimization problem in Alg. 1 and the procedure for basis dimension selection in Alg. 2.

Algorithm 1 AEB algorithm for topology optimization

for i=1:4 **do**
  Compute spatial coefficients $[\mu^{(i)}]_e$ and select initial maximum basis dimension with ℓ_{max}
  Compute $[\Phi^{(i)}_{\ell_{max}}]$ from EVP (Eq. 24)
  Orthnormalize $[\Phi^{(i)}_{\ell_{max}}]$
  Select basis dimension $\ell^{(i)}$ and compute initial guess $\boldsymbol{b}_0^{(i)}$ from (Alg. 2)
  Set $k = 0$
  while not converged **do**
    Solve forward problem (Eq. 4)
    Solve adjoint problem (Eq. 18)
    Evaluate objective: $\tilde{\mathcal{J}}(\boldsymbol{b}_k^{(i)})$
    Evaluate gradient: $\tilde{\mathcal{J}}'_{\boldsymbol{b}}(\boldsymbol{b}_k^{(i)})$
    Compute design update step
    Check convergence criteria
    k = k+1
  end while
end for
Update projection slope ζ and DWP coefficient α_0

Algorithm 2 Basis dimension selection and initial guess generation

Given: Pass (i), $\boldsymbol{\beta}^{(i-1)}$, $[\Phi^{(i)}]$, ϵ_{tol} OR $\{kmax, k_{min}\}$
if $i = 1$ **then**
  Compute wavelengths $\{w_i\}$ from eigenvalues $\{\lambda_i\}$, $i = 1..\ell_{max}$
  Truncate basis w.r.t. wavelength tolerances $\{k_{max}, k_{min}\}$
else
  for $j = 1 : l_{max}$ **do**
    Compute $\boldsymbol{b}_{0,j}^{(i)}$ using L^2 projection of $\boldsymbol{\beta}^{(i-1)}$ onto basis $[\Phi_j^{(i)}]$ (Eq. 49)
    Compute L^2 relative projection error ϵ_j (Eq. 54)
    Compute marginal L^2 error reductions $\hat{\epsilon}_j$ (Eq. 55)
  end for
  Reorder eigenfunctions with respect to $\hat{\epsilon}_j$
  Compute relative marginal error decreases $\{c_j\}$ (Eq. 56)
  Select min j s.t. $c_j \leq \epsilon_{tol}$, and $l^{(i)} = j$
  Compute initial guess $\boldsymbol{b}_0^{(i)} = \boldsymbol{b}_{0,j}^{(i)}$ from Eq. 49
end if

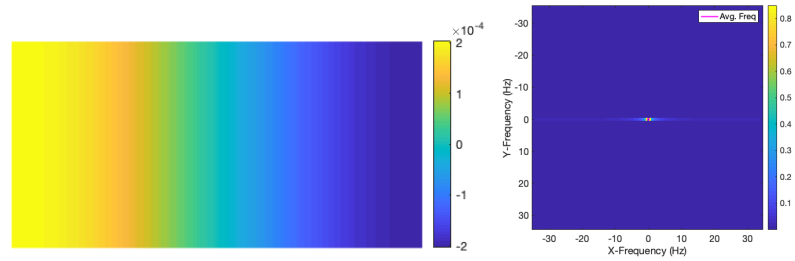

(a) Eigenfunction ϕ_2 (b) Spatial FT of ϕ_2

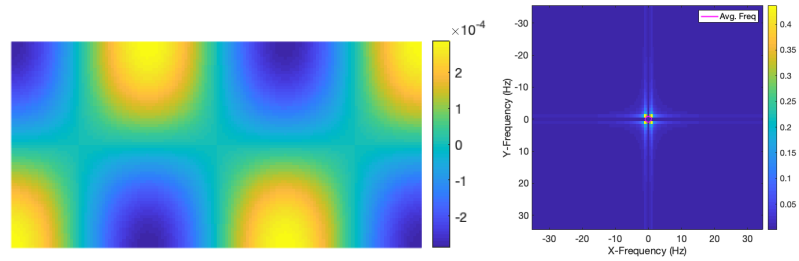

(c) Eigenfunction ϕ_8 (d) Spatial FT of ϕ_8

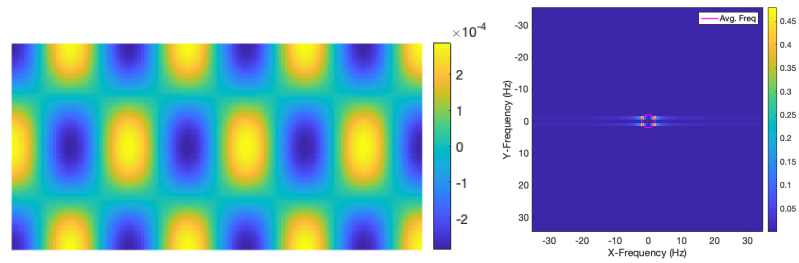

(e) Eigenfunction ϕ_{32} (f) Spatial FT of ϕ_{32}

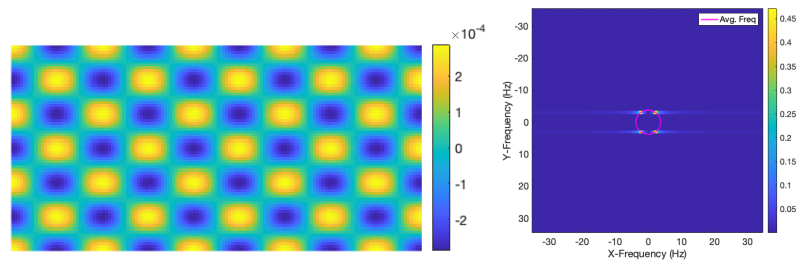

(g) Eigenfunction ϕ_{100} (h) Spatial FT of ϕ_{100}

FIGURE 8 Laplacian eigenfunctions of a 2×1 rectangular MBB domain and corresponding amplitude spectra of SFFT, shown in $x - y$ frequency space. Circle plot (in pink) indicates dominant frequency predicted from eigenvalues.

5 | DESIGN STUDIES

In this section, we demonstrate the performance of the AEB method in solving topology optimization problems. We examine the effects of basis dimension upon solution quality and the solution improvement gained through basis adap-

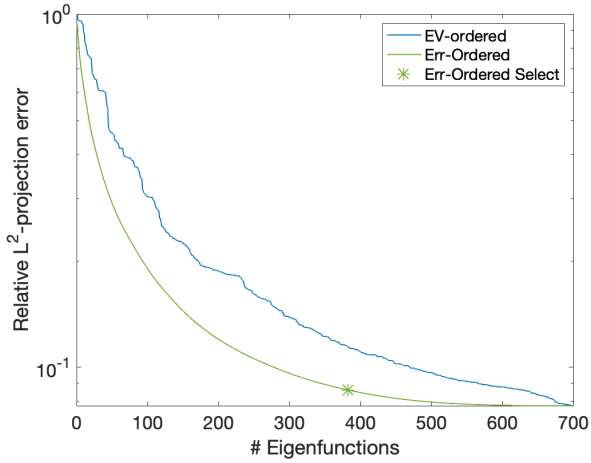

FIGURE 9 Relative L^2-error between previous fictitious-density solution and its projection upon new bases with increasing dimension. Reordering of eigenfunctions according to respective L^2-projections, rather than by eigenvalue, prioritizes selection of basis functions with largest contributions to current solution.

tation. We benchmark our results against results from conventional density-based design methods (CDM), examining structural performance comparisons and potential computational cost savings. We furthermore provide guidance on implementation of the parameter continuation schemes that enable consistent convergence of the AEB method to 0-1 solutions. We discuss implementation details in Appendix A.

We will consider various prototypical design cases for linear-elastic topology optimization. These include the "MBB-beam", shown in Figure 10a, which represents a simply-supported beam subject to a midspan loading. Under symmetry conditions, only half of the structural domain is modeled. We will consider the minimization of static downward displacement at the midspan node (indicated in blue). Next is a cantilever beam, shown in Figure 10b, subject to fixed-support at its left edge and a downward traction along a portion of the right edge. We solve for displacement-minimization of the beam end measured at the location of force application (in blue).

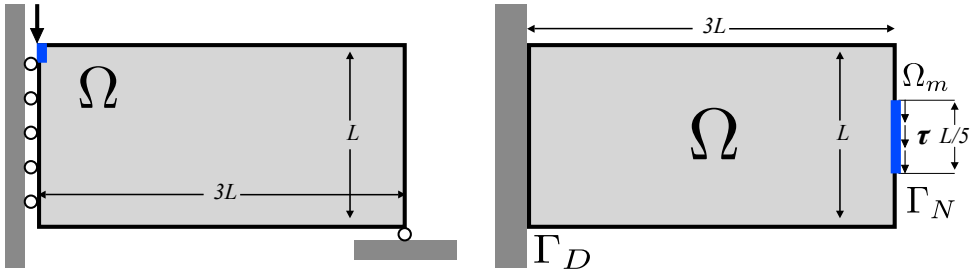

(a) MBB beam design domain.

(b) Cantilever beam design domain.

AEB examples are implemented in a two-dimensional FE MATLAB code and solved with the MATLAB `fmincon` interior-point method [19]. For comparison purposes, a conventional density method is also implemented to bench-

mark solution quality, though using the MATLAB globally-convergent Method of Moving Asymptotes algorithm to solve the optimization problem [20]. We evaluate structural performance of the designs, as measured by structural objectives and gray fraction, as well as the convergence behavior and the effects of various algorithmic parameters on the solution. We compute the gray fraction f_g, as introduced in [21] to measure the remaining fraction of gray material in the analysis density field, as

$$f_g := \frac{4}{V_\Omega} \sum_e \int_{\Omega_e} (h_e)(1 - h_e) d\Omega_e.$$

5.1 | Study: Basis Dimension

We first evaluate the effect of initial basis dimension upon solution quality with a series of designs whose bases are truncated with respect to different wavelength-thresholds. We investigate the design of a 3×1 cantilever beam, using 180×60 bilinear, four-node elements under plane-stress conditions and subject to a 50% volume fraction constraint. Fictitious elastic material properties use a two-phase interpolation, with void phase properties $\{G_0, \kappa_0\} = \{1 \times 10^{-5}, 4 \times 10^{-5}\}$ and solid phase $\{G_1, \kappa_1\} = \{1, 4\}$.

We use only the eigenfunctions of the Laplacian operator ($[\mu]_e = [I]$) for our design basis, and compute each eigenfunction's mean spatial wavelength from its corresponding eigenvalue. For the first 4 design examples, we truncate the design subspace based upon decreasing minimum wavelength limits, defined with respect to the domain height L, so that smaller wavelength limits produce design subspaces spanned by larger numbers of basis functions. For the two final designs, we perform "band-pass" truncation, eliminating both low and high frequency eigenfunctions from the basis in two different ranges. We use continuation schemes for the projection slope and the regularization coefficient in the objective. We initialize $\zeta = 2$ and apply an update factor of 1.5 every 100 iterations, or upon reaching a local minimum, reaching a maximum $\zeta = 15.1$, while we initialize $\alpha_0 = 1e-4$ and apply an update factor of 1.2 each time ζ is updated. Each example is limited to a maximum of 750 total iterations; in the interior point method, multiple function-evaluations may be necessary within a iteration, so we also report function evaluation count to reflect true computational cost. Design statistics, including final displacement objective and gray fraction, are reported in Table 1. Figure 12 shows the obtained designs.

Trial	k_{min}, k_{max}	# of EF	Obj	f_g	DWP	Iter Count	Func Count
1	$\{0.4L, -\}$	63	9.257e+01	0.0778	1.018e+01	703	742
2	$\{0.3L, -\}$	110	8.360e+01	0.0902	9.071e+00	629	669
3	$\{0.2L, -\}$	239	7.604e+01	0.0520	2.156e+00	597	630
4	$\{0.1L, -\}$	699	7.336e+01	0.0240	1.098e+00	439	490
5	$\{0.1L, 0.4L\}$	636	1.173e+02	0.0324	3.105e+01	658	750
6	$\{0.1L, 0.2L\}$	459	2.034e+02	0.0297	1.092e+02	620	669

TABLE 1 Eigenspace Basis Design: effects of dimension size upon structural performance. Wavelength limits k_{max} or $\{k_{max}, k_{min}\}$ are set with respect to the domain height $L = 1$. Each design was produced in 600 iterations.

The EB method successfully obtains acceptable cantilever designs using design subspaces nearly two orders-of-

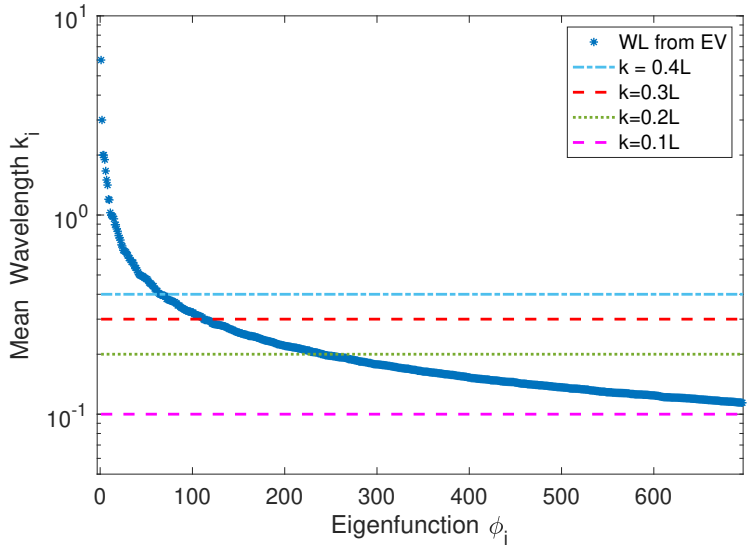

FIGURE 11 Principal average wavelengths associated with eigenfunctions, computed from eigenvalues, depict a monotonic decrease in wavelength for eigenfunctions associated with higher eigenvalues. Dashed lines show different cutoff thresholds used in design studies.

magnitude smaller than a conventional, element-wise density parameterization. Objective evaluations, measuring structural displacements, indicate the performance of each EB optimization: we observe that the lower dimensional EB solutions (e.g. Trial 1) obtain large displacement objective values, while solutions obtained with expanded EB subspaces (e.g. Trial 4) are able to achieve decreased displacement levels. We do observe structural performance improvements leveling off, however, for larger basis dimensions. The design with the largest basis (trial 4) converges to a design with only slightly superior structural performance than the solution using hundreds fewer basis functions (trial 3), suggesting that including many high-frequency EF's has diminishing effect on improving solution accuracy. Band-pass limited designs (trials 5 and 6) recorded the largest objective evaluations, as these structures were restricted from developing large length scale features that most improve to structural stiffness; they also develop extraneous floating features, due to the restriction in the void length scale, that do not contribute to structural performance but do detract from the volume utilization.

We can confirm the low-pass and band-pass filtering induced through basis truncation by inspection of the amplitude spectra of the SFFT's of solutions 4 and 6, as shown in Fig. 13. In both cases, spectral amplitude densities are concentrated within the maximum-frequency radius induced by the wavelength-threshold criteria. Furthermore, truncation of the low index eigenfunctions, as shown in the SFFT of the Trial 6 band-pass solution (Fig. 13b), restricts the solution from containing low-frequency/large wavelength content, with the amplitude content nearly bounded between the two frequency threshold frontiers. This filtering is achieved while eliminating two linear solutions or convolutions from each objective function evaluation as would be required for the low-pass PDE-filter, and potentially four linear solutions for a band-pass PDE-filter [18].

We see differing structural qualities and complexity arising from different basis truncation choices. Solution complexity generally increases the complexity of structural designs, with more numerous, smaller features and holes pre-

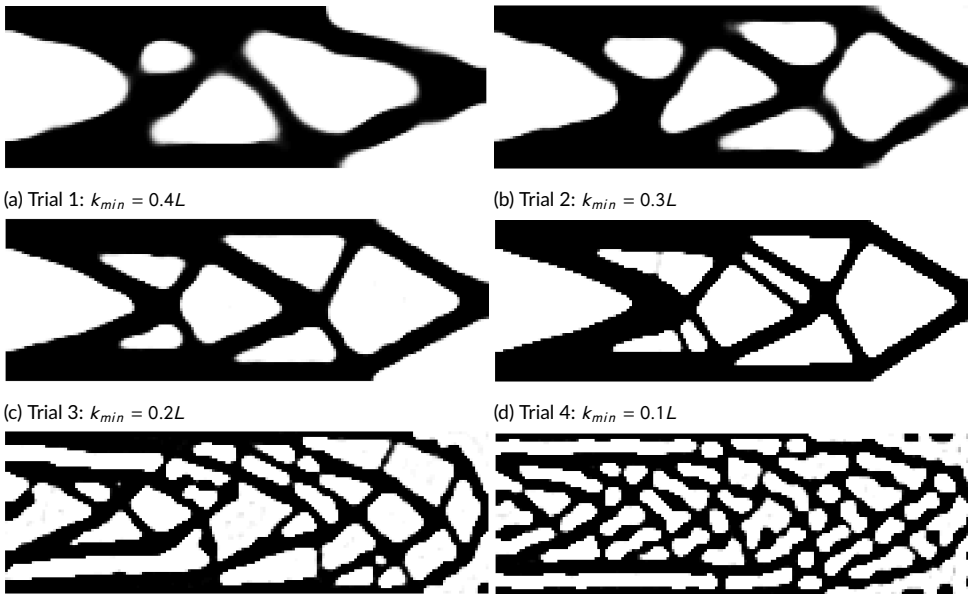

(a) Trial 1: $k_{min} = 0.4L$ (b) Trial 2: $k_{min} = 0.3L$

(c) Trial 3: $k_{min} = 0.2L$ (d) Trial 4: $k_{min} = 0.1L$

(e) Trial 5: $\{k_{min}, k_{max}\} = \{0.4L, 0.1L\}$ (f) Trial 6: $\{k_{min}, k_{max}\} = \{0.4L, 0.1L\}$

FIGURE 12 Cantilever beam designs with Laplacian eigenfunction bases truncated at different wavelength thresholds.

cipitating in designs with larger subspace dimension. Structural designs obtained with these Laplacian eigenfunction bases, especially for lower dimensional subspaces, tend to posses rounded, organic features. The organic quality of the structural solutions are due to the relatively poor capacity of sinusoidal eigenfunctions, especially with large wavelength, to capture straighter and smaller structural members. Furthermore, though all problems were subject to the same projection and regularization continuation schemes, the higher-dimensional designs were able to obtain lower gray-fractions, as the higher-frequency bases can capture sharper boundaries. Asymmetries in the designs likely arise from potential asymmetries in the selected basis members; symmetries in design can be enforced if desirable, e.g. by suitable BCs in the EVP definition. Band-pass limited structures develop almost cellular-appearing quality, with numerous holes arising from the restriction of the solution to high-frequency oscillating bases.

5.2 | Study: Length Scale Control

We explicitly demonstrate the use of basis truncation as means for minimum and maximum length scale control in the next example problem. We design a two-dimensional, plane-stress square structure under uniform tension, for which we expect the solution to be an assembly of vertical bars. We use a 1×1, 80 x 80 bilinear FE discretization of the domain, for which the top edge has fixed boundary conditions while the bottom edge experiences a uniform, downward traction. The analytical domain is shown in Figure 14. Fictitious elastic material properties use a two-phase interpolation, with void phase properties $\{G_0, \kappa_0\} = \{1 \times 10^{-5}, 4 \times 10^{-5}\}$ and solid phase $\{G_1, \kappa_1\} = \{1, 4\}$. We utilize a logistic-slope projection scheme, with initial $\zeta = 2$ and an update factor of 1.5 applied every 100 iterations, with a maximum 400 iterations. We maintain a constant DWP weighting $\alpha_0 = 1 \times 10^{-5}$.

We perform three designs, each with a unique band-pass basis truncation criteria defined with respect to the

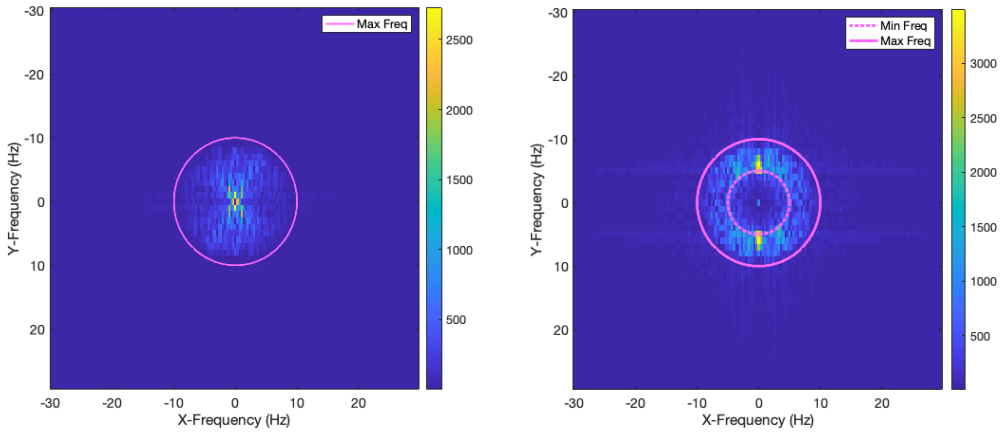

(a) SFFT of Trial 4 design

(b) SFFT of Trial 6 design

FIGURE 13 Spatial FFT of β fields for Trial 4 and 6 solutions; circles indicate equivalent maximum (and minimum) frequency thresholds applied through basis truncation.

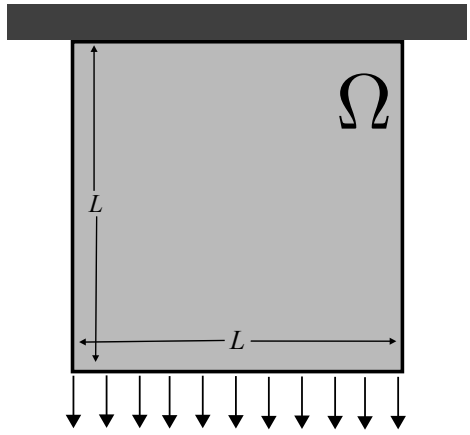

FIGURE 14 Structural domain under tension for length-scale design study.

structure length-scale L. Designed structures are shown in Figure 15. In example (a), we select basis functions with wavelengths $k \in [0.20, 0.30]L$. In example (b), we select basis functions with wavelengths $k \in [0.15, 0.20]L$. Finally, in example (c), we select basis functions with wavelengths $k \in [0.10, 0.15]L$.

We observe that bandpass-designed structures exhibit features with "wavelengths"–transition from void to solid consistent with the wavelengths chosen in the eigenfunction bases. For a band-pass truncation with mean wavelength $\bar{k}$, we expect approximately $1/\bar{k}$ vertical bars in the solution; the resulting structural qualities in each design are consistent with these wavelength-predictions. Namely, we see approximately 4 bars in Fig. 15a, 6 in Fig. 15b, and 8 in Fig. 15c. Furthermore, we can observe that resulting feature size, in these simple 1-D tension examples, is

approximately $\frac{1}{2}k$, which can be used as a rough criteria for wavelength-truncation criteria with respect to desired feature size. Irregularities in the design–fluctuations in the feature width or joining of the parallel bars–likely occur due to the non-exact frequency-content filtering performed via basis truncation. Nevertheless, we show that truncation of initial eigenfunction basis effectively allows for length scale control.

(a) k_l=[0.2, 0.3]L (b) k_l=[0.15, 0.2]L (c) k_l=[0.1, 0.15]L

FIGURE 15 Structures designed for tensile-stiffness, using band-pass basis truncation for length-scale control.

5.3 | Study: Single versus Adapted Eigenspace Bases

We next evaluate the performance of the basis adaptation strategy for its solution quality, basis dimension compression, and computational cost. We design cantilever and MBB beams using the proposed AEB strategy, and compare results both to the original Laplacian eigenbasis solution and results obtained with a conventional density based method. In each case, we use a 3×1 domain modeled with 180×60 bilinear elements under plane-stress assumptions and subject to a 50% volume fraction constraint. The fictitious material properties used in each model include void phase properties $\{G_0, \kappa_0\} = \{1 \times 10^{-5}, 4 \times 10^{-5}\}$ and solid phase $\{G_1, \kappa_1\} = \{1, 4\}$.

We solve four successive optimization problems in each AEB design case, using the sequence of AEB computed from the four proposed eigenvalue problems. The first problem is initialized as a homogeneous density field $\boldsymbol{\beta} = 0$ (i.e. $\boldsymbol{b} = 0$). In subsequent passes, we construct the adapted-EVP operators as defined in Eq. 40 through Eq. 43 using the pseudo-density solution from the previous optimization pass. We initialize the design variable as the projection of the previous pseudo-density solution upon the newly-computed basis; we conduct two trials each for the MBB and cantilever beams, using relative L^2-error decrease tolerances of $\epsilon_{tol} = 0.001$ or $\epsilon_{tol} = 0.005$ to select the adapted basis dimensions. Each optimization pass is solved to a gradient tolerance of 1×10^{-6}, function decrease tolerance of 1×10^{-6}, a step-size tolerance of 1×10^{-4}, or a maximum iteration limit. We allow the first pass to proceed for three continuation-updates (maximum 300 iterations), and each subsequent pass for maximum 100 iterations. We employ an identical continuation strategy as in the previous studies for both the projection slope and regularization coefficient: we initialize the penalty coefficient $\alpha_0 = 1 \times 10^{-4}$ to which we apply an update factor of 1.2 after each 100 iterations or upon reaching a local minimum. We initialize the logistic slope parameter $\zeta = 2$ and increase by a factor of 1.5 every 100 iterations, or upon reaching a local-minimum, throughout the optimization procedure. We enforce a $0.1L$ wavelength limit upon the Laplacian basis, resulting in an initial basis dimension of 700.

To evaluate the quality of AEB solutions, we solve a conventional density TO problem with the same initial density ($h(\boldsymbol{\beta}) = 0.5$) and under the same volume constraint. Our CDM comparison problem enforces element-wise the

densities $0 \leq \beta_e \leq 1$ and uses a Helmholtz filter with radius $r = 0.0125$ (this radius provides length-scale control approximately equivalent to the AEB wavelength-threshold criteria). We use a Heaviside projection continuation scheme [15], centered at 0.5, set with initial slope $\zeta = 1$, and multiplied by 1.8 every 100 iterations. These CDM solutions are obtained using the MATLAB implementation of the MMA solver [20].

The structural solutions from the CDM problem and four AEB passes are shown in Figure 16 for the cantilever beam and in Figure 17 for the MBB beam. Tables 2 and 5 report the final structural displacement objective evaluation, gray fraction, DWP term value, and total function evaluation count obtained for each solution. Tables 3 and 4 show the objective term evaluations, basis dimension, and computational cost statistics from each optimization stage for the cantilever designs, while Tables 6 and 7 show results for the MBB designs. We observe that structural displacement objectives decrease with each successive adapted pass, as both the continuation schemes and the adapted bases enable convergence to well-defined structures with minimal intermediate gray material. Final displacement results for the trial 1 cantilever beam design (shown in Fig. 16g) outperform the best results obtained in the previous dimension-study using the single Laplacian eigenfunction basis (Cantilever AEB Trial 1: 7.320e+02 vs. Cantilever Laplacian Trial 4: 7.336e+02), under identical continuation schemes and convergence criteria and in fewer (433 vs. 471) iterations and function evaluations (448 vs 499).

AEB-obtained solutions furthermore achieve objective values comparable to those obtained by solutions using conventional density based methods. Structural displacement objectives calculated for the final AEB solutions are within 2% of the results achieved by structures using conventional methods (with the AEB-MBB Trial 1 design actually outperforming the CDM result). We obtain these structures from design spaces that are over two orders of magnitude smaller than the conventional element-wise discretization of the design variable, and an additional order of magnitude smaller than the original Laplacian EB. AEB results are also obtained in fewer iterations and function evaluations than the CDM solution. We do note different optimization algorithms are used for the different cases and therefore exact comparison is difficult, but comparison of the number of function evaluations (and thus the number of linear solution evaluations) can roughly compare overall computational cost. Though the AEB strategy requires the solution of four eigenvalue problems, its per-function-evaluation cost is significantly lower than the CDM method: both methods require the solution of the forward and adjoint problems each function evaluation, but the CDM method requires two additional filtering linear-solutions.

Value	AEB 1: $\epsilon_{tol} = 0.001$	AEB 2: $\epsilon_{tol} = 0.005$	CDM
Objective	7.325e+01	7.474e+01	7.204e+01
Gray Frac	1.336e-02	1.925e-02	1.735e-02
DWP	3.031e-01	3.820e-01	-
Total Iter	433	457	600
Total Func Count	448	532	600

TABLE 2 Final optimization results for cantilever beam designs, comparing AEB solutions to CDM results.

As reported in Table 5, both the DWP evaluation and the basis dimensions in the adaptive passes are also consistently reduced throughout the optimization process. Decreasing DWP evaluation signifies clustering of the solution near ± 1 values; such clustering enables effective utilization of the AEB to represent the increasingly piece-wise constant pseudo-density field with low dimension. The AEB solutions yield lower final DWP evaluations than the

Value	Pass 1	Pass 2	Pass 3	Pass 4
# EF	700	383	159	84
Objective	7.8758e+01	7.5433e+01	7.3943e+01	7.3258e+01
DWP	4.128e+00	1.238e+00	4.433e-01	3.031e-01
Iter Count	261	68	50	54
Func Count	271	71	51	55

TABLE 3 AEB Cantilever Trial 1: design results for successive AEB passes.

Value	Pass 1	Pass 2	Pass 3	Pass 4
# EF	700	140	47	23
Objective	7.8758e+01	7.7140e+01	7.5585e+01	7.4741e+01
DWP	4.128e+00	1.486e+00	6.252e-01	3.820e-01
Iter Count	261	41	99	56
Func Count	271	42	146	73

TABLE 4 AEB Cantilever Trial 2: design results for successive AEB passes.

Value	AEB 1: $\epsilon_{tol} = 0.001$	AEB 2: $\epsilon_{tol} = 0.005$	CDM
Objective	1.1960e+02	1.2281e+02	1.200e+02
Gray Frac	1.578e-02	2.4862e-02	1.703e-02
DWP	3.487e-01	5.1641e-01	-
Total Iter	382	426	600
Total Func Count	433	446	600

TABLE 5 Final optimization results for MBB beam designs, comparing AEB solutions to CDM results.

Value	Pass 1	Pass 2	Pass 3	Pass 4
# EF	700	435	175	93
Objective	1.3550e+02	1.2496e+02	1.2097e+02	1.1960e+02
DWP	1.276e+00	6.315e-01	4.010e-01	3.487e-01
Total Iter	235	59	44	44
Total Func Count	247	60	54	60

TABLE 6 AEB MBB Trial 1: design results for successive AEB passes.

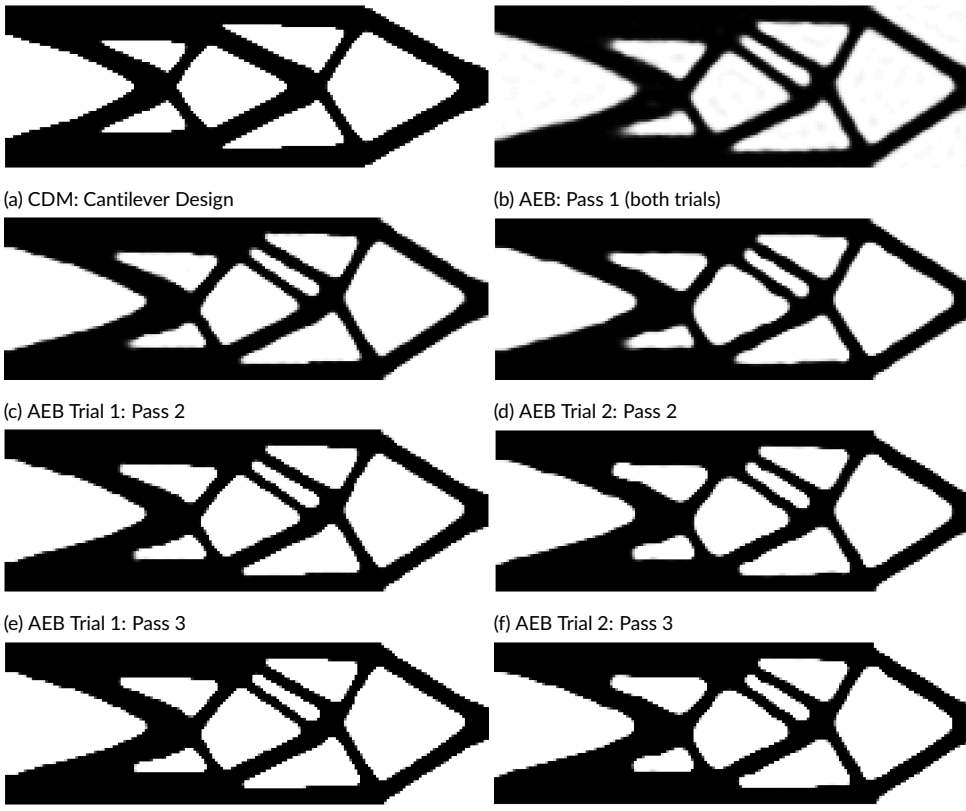

(a) CDM: Cantilever Design

(b) AEB: Pass 1 (both trials)

(c) AEB Trial 1: Pass 2

(d) AEB Trial 2: Pass 2

(e) AEB Trial 1: Pass 3

(f) AEB Trial 2: Pass 3

(g) AEB Trial 1: Pass 4

(h) AEB Trial 2: Pass 4

FIGURE 16 Design results for cantilever beams produced through four successive adaptive basis constructions, compared with design obtained through conventional density-based methods. Trial 1 uses L^2-error decrease tolerances of $1e-3$ and Trial 2 uses $5e-3$.

Laplacian basis (e.g. AEB Cantilever Trial 1: 3.031e-01 vs. Laplacian Cantilever Trial 4: 1.098e+00), reflecting the improved ability of the adapted bases to conform to piece-wise constant values. The compression is further evidenced in Figures 18a through 18d, which show the relative L^2-error achieved by projections of the final pseudo-density design from each pass onto the next adapted (reordered) basis, with increasing dimension. Error decreases quickly using the adapted bases, and more rapidly with each successive pass; for the higher projection-error tolerances, we are able to decrease the basis dimension by over an of magnitude between the initial and final passes (from 700 to 23 and 31, for cantilever and MBB Trial 2 designs). We also observe that the error tolerance used strongly affects the basis dimension selected and resulting structural solution. Comparing Trial 1 and 2 results in both design scenarios, we observe tighter error tolerance yields naturally larger bases but produces improved final solutions; however, with slackened error tolerance, we trade only minor performance decreases ($\approx$ 2.4% for both cases) for improved final basis compression ($> 3\times$ smaller). Final structural solutions for Trial 2 (Fig. 16h and 17h) have qualitatively identical features to the solutions obtained with the larger bases, though with slightly-rounder features.

We generally observe solutions at each stage of the adaptive process develop sharper, smoother, and straighter features than solutions from the initial pass. The sinusoidal quality of the initial Laplacian EF's and the combined small-

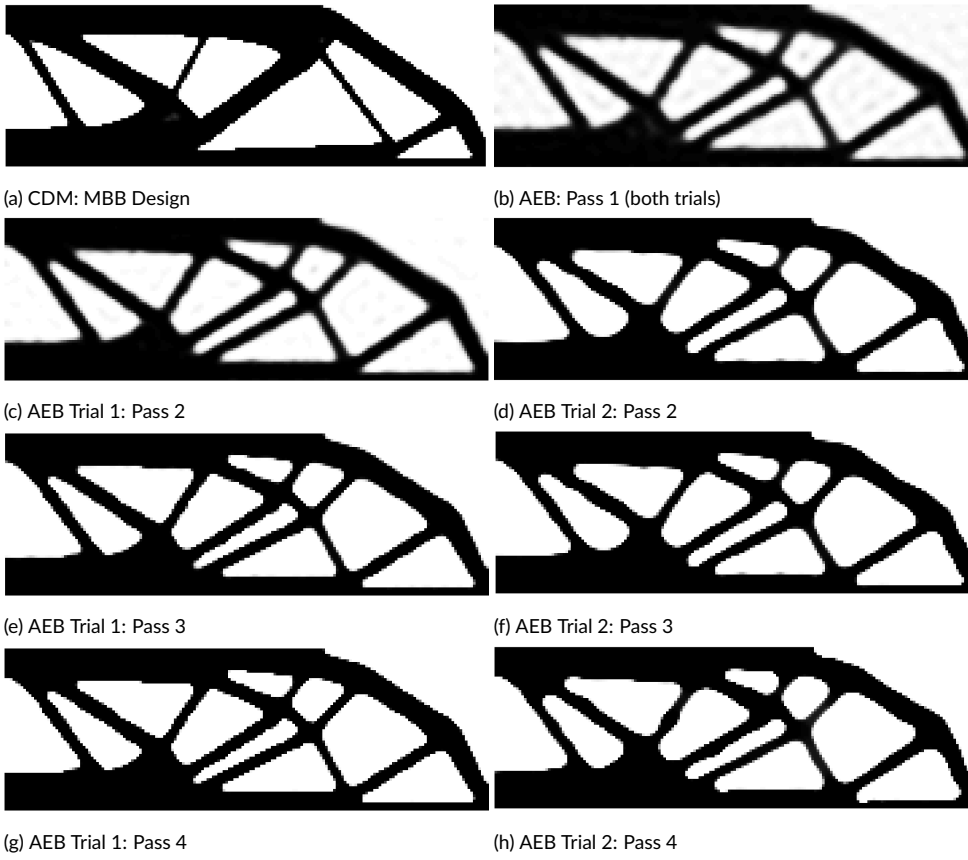

(a) CDM: MBB Design

(b) AEB: Pass 1 (both trials)

(c) AEB Trial 1: Pass 2

(d) AEB Trial 2: Pass 2

(e) AEB Trial 1: Pass 3

(f) AEB Trial 2: Pass 3

(g) AEB Trial 1: Pass 4

(h) AEB Trial 2: Pass 4

FIGURE 17 Design results for MBB beams produced through four successive adaptive basis constructions, compared with design obtained through conventional density-based methods. Trial 1 uses L^2-error decrease tolerances of $1e-3$ and Trial 2 uses $5e-3$.

projection slope and small regularization value used in the first pass contribute to the rounded, diffuse shape quality of Pass 1 solutions (Fig. 17b & 16b). In the adaptive bases, concentrated variation at the structural-void boundary enables refinement of the edges between void and solid. Trial 2 designs, with restricted basis dimensions, do display features with rounded or variable widths. Asymmetries in AEB solutions (e.g. Fig. 16g and Fig. 16h) seemingly develop during the first pass due to the oscillatory or asymmetrical nature of the initial EF's.

6 | DISCUSSION & CONCLUSIONS

We have presented a new design dimensionality-reduction approach for density-based topology optimization problems. Our adapted eigenfunction basis is an effective proxy for traditional density based design parameterization: solutions achieve structural performance metrics on par with conventional based density methods while parameterized by design spaces multiple orders of magnitude smaller. The EB representation not only allows for drastic reduction in dimensionality of design space, but also imposes implicit regularization of the design field, providing a successful

Value	Pass 1	Pass 2	Pass 3	Pass 4
# EF	700	189	61	31
Objective	1.3550e+02	1.2776e+02	1.2441e+02	1.2281e+02
DWP	1.276e+00	1.049e+00	6.871e-01	5.164e-01
Iter Count	235	68	63	55
Func Count	247	70	73	56

TABLE 7 AEB MBB Trial 2: design results for successive AEB passes.

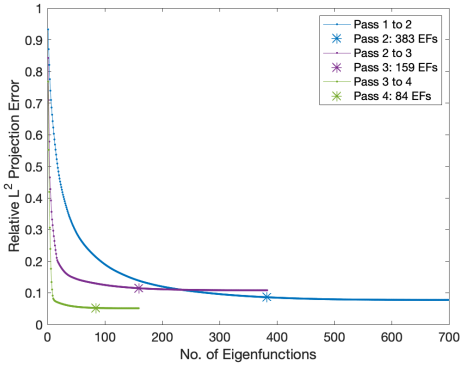

(a) Cantilever Design: Trial 1

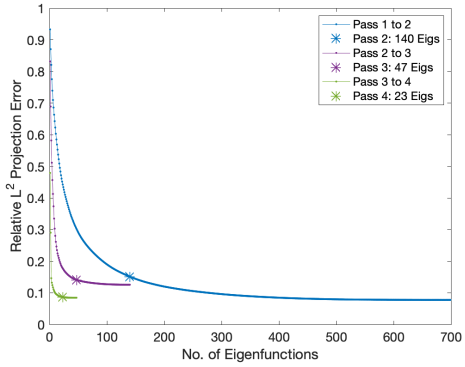

(b) Cantilever design: Trial 2

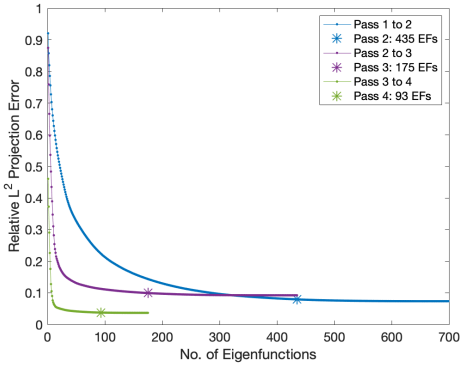

(c) MBB Design: Trial 1

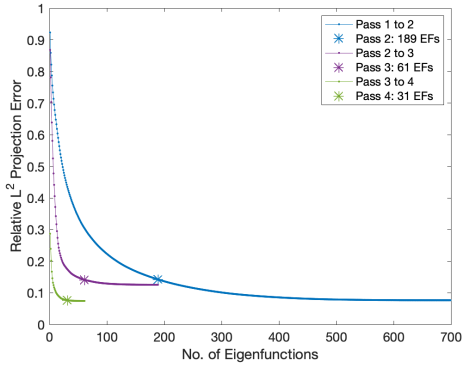

(d) MBB design: Trial 2

FIGURE 18 Relative L^2 projection errors, computed with bases of increasing dimension. Stars indicate basis dimension selected. Increased error tolerances in Trial 2 examples allow for decreased dimension selections.

subspace in which to represent the design. Representation of the fictitious-density as the sum of eigenfunctions, and projection onto the logistic function, removes the computational expense of element-wise 0-1 bound constraints and

density-filtering schemes. Convergence to finite basis coefficients is secured through the use of a double well potential regularization term, which by penalizing both large and small magnitude fictitious-densities encourages convergence of the eigenfunction-expanded solution to ± 1 values, and thereby to finite basis coefficients.

Through the adaptive strategy proposed, the design basis is updated to represent the current solution trajectory, enabling further compression of the design space and acceleration of the optimization solution. Meanwhile, the double-well potential regularization encourages this effective compression, as the fictitious-density solutions are steered towards bimodal, piecewise constant fields which may be approximated in low-dimensional form using the adapted eigenfunctions. The four-stage adaptive sequence proposed works well to reduce basis dimensionality iteratively and ultimately obtain good-quality structural solutions; further basis compression may be obtained through additional, or more frequent, adaptive passes. The resulting small-dimensional design space enables our use of optimization algorithms (the primal-dual interior-point method) typically impractical in conventional TO problems due to their high dimensionality. For example, the primal-dual interior point method in MATLAB requires the factorization of a $n_{var} \times n_{var}$ Hessian-approximation to compute design step updates, where n_{var} is the number of design variables [19], in which case the smaller AEB dimension is clearly favorable.

An additional, unique benefit of the eigenfunction basis truncation is its resulting implicit control over solution length scale. We have shown the effect of Laplacian eigenfunction truncation of the initial basis operates with similar effect to either low-pass or band-pass filter operations, and thus operates as means of controlling solution length scale. We see from these results, and in our general experience, that structural topology is generally defined in the first optimization pass, as the initial solution using the Laplacian EB determines the general solution form, including the size and numbers of structural features. The adapted bases are adept at capturing and perturbing the current solution, though may not be equipped to represent dramatically different structural forms. New features may still evolve and old features disappear during the adapted passes, but drastic shifts in solution character are unlikely during the later adaptive passes. We also note that band-pass length-scale control, especially restriction of the solution to high frequency content, is not always preserved in subsequent passes; a solution featuring only small-scale features, for example, may redevelop larger features once the adapted bases are used. Further study is needed to maintain band-pass length scale control in the adaptive passes.

Several additional questions may be pursued to maximize the utility of the AEB method. We have not established explicit uniqueness or mesh-independence of solutions, as designs using the same dimension AEB, but with different mesh discretization or eigenfunction members, can converge to qualitatively different designs. This behavior likely owes to slight numerical differences in the eigenfunctions computed for different meshes, so that designs on different meshes are effectively confined to different eigenfunction subspaces. However, constraint of the spatial variation wavelength to a given level does generally result in qualitatively similar structural solutions. Next, as the AEB method provides global, rather than element-wise, parameterization of the design field, local element-wise constraints are not applicable. Thus, methods that impose local constraints or operations, including strict length-scale, such as morphological filters (e.g. [22]) or maximum-overhang (e.g. [23]) onto TO designs need redevelopment in the AEB context.

Additional methods to improve the computational performance of the AEB method may likewise be pursued. Sparse storage of the eigenfunctions may be an attractive method to reduce memory costs and implement the method in parallel, as suggested in [8]. As higher-index eigenfunctions have only localized regions of variation and near-zero values elsewhere, EF's may reasonably be stored in a sparse format, with only non-zero values and associated element-indices. Such storage format would save memory-costs in a parallelized, domain decomposed implementation. Mesh adaptivity schemes have been explored for other adaptive eigenspace inversion formulations [10] and would prove useful in the present framework for improved refinement of boundaries between material phases. Next, the use of

ubiquitous MMA-solvers for TO problems requires additional care for the AEB formulation, primarily because users must supply design variable bounds to initialize the solver. Initial steps in MMA solvers risk pushing the basis coefficients associated with high-frequency eigenfunctions to the supplied bounds, causing premature convergence to nearly-random, black-white patterns. Aggressive continuation strategies and tailored eigenfunction coefficient bounds are necessary for successful implementation of the AEB method with MMA-solvers.

We view the AEB method as a promising alternative to conventional element-wise parameterizations of the design field. The method's main benefits are its significant design dimensionality reduction, its replacement of conventional density filtering operations, and its implementation of simple length scale control. Operation of the AEB method with a mesh-adaptation scheme will further emphasize the improved resolution of the eigenfunction variation near large-gradient regions in the solution field. We predict the AEB method may be used in topology optimization problems for a variety of physics applications.

7 | ACKNOWLEDGEMENTS

Acknowledgements should include contributions from anyone who does not meet the criteria for authorship (for example, to recognize contributions from people who provided technical help, collation of data, writing assistance, acquisition of funding, or a department chairperson who provided general support), as well as any funding or other support information.

8 | CONFLICT OF INTEREST

You may be asked to provide a conflict of interest statement during the submission process. Please check the journal's author guidelines for details on what to include in this section. Please ensure you liaise with all co-authors to confirm agreement with the final statement.

A | IMPLEMENTATION DETAILS

We discuss a few details related to operation of the AEB method for topology optimization.

A.1 | Continuation Schemes & Effects of Double-Well Potential Term

In our formulation, convergence to successful black-white designs depends on an interplay between the logistic projection slope and the regularization coefficient magnitude. The combination of the logistic projection and the DWP regularization ensures that designs satisfy minimum standards: that analysis densities reside between 0-1 and that the EF-coefficient solutions do not approach unbounded values. However, the combination of the slope value and regularization weighting will strongly affect the convergence to good quality solutions. Continuation strategies are ultimately useful to control convergence of the solution to optimal, near 0-1 analysis density designs.

A successful continuation strategy for the AEB method initializes both the logistic slope and the regularization coefficient at small values (e.g. $\zeta = 2, \alpha_0 = 1e-4$) and gradually increases both values. The initial development of an advantageous topology pattern–albeit still with intermediate densities–can permit subsequent basis adaptations to emphasize these developing structural-void boundaries and obtain high-quality solutions in low-dimensional form. We

find that only modest increase factors of the DWP weighting are necessary to provide the desired bimodal clustering; continuation of the slope parameter to large values ($\zeta > 10$) is more important since we want projected densities at $\beta = \pm 1$ to be sufficiently close to 0 or 1. Though we have not established explicit criteria for selection of the DWP weighting coefficient, it appears to be connected to the overall lengthscale desired for the structure.

A.2 | Algorithm Selection

We may solve the PDE-constrained design problem using standard nonlinear programming algorithms. AEB design studies in this report use an interior-point method as implemented in `MATLAB fmincon`, choosing a full-step strategy and assigning KKT-norm, step-norm, and function-step convergence criteria [19]. The EVP (Eq. 23) is computed with the `MATLAB` eigenvalue solver, which uses Lanczos iteration and determines the eigenvectors associated with a lowest subset of eigenvalues of the discretized EVP. We note the AEB formulation may alternatively use the Method of Moving Asymptotes (MMA) method, the popular algorithmic option for solving constrained minimization problems in density-based TO [20]. However, our formulation does pose some issues for MMA solvers. Successful operation of the MMA optimizer using the AEB approach requires user-supplied, initial artificial design variable bounds. We do not have a priori estimates of the values (or magnitudes) the basis coefficients should take, but we may provide artificial design bounds in reference to the values from an initial eigenfunction coefficient guess, for example. Larger regularization coefficients may also be useful to avoid immediate convergence to random, 0-1 solutions.

references

[1] Sigmund O, Petersson J. Numerical instabilities in topology optimization: a survey on procedures dealing with checkerboards, mesh-dependencies and local minima. Structural optimization 1998;16(1):68–75.

[2] Bourdin B. Filters in topology optimization. International journal for numerical methods in engineering 2001;50(9):2143–2158.

[3] Lazarov BS, Sigmund O. Filters in topology optimization based on Helmholtz-type differential equations. International Journal for Numerical Methods in Engineering 2011;86(6):765–781.

[4] Guest JK, Smith Genut LC. Reducing dimensionality in topology optimization using adaptive design variable fields. International journal for numerical methods in engineering 2010;81(8):1019–1045.

[5] Huang W, Sun W. Variational mesh adaptation II: error estimates and monitor functions. Journal of Computational Physics 2003;184(2):619–648.

[6] Lambe AB, Czekanski A. Topology optimization using a continuous density field and adaptive mesh refinement. International Journal for Numerical Methods in Engineering 2018;113(3):357–373.

[7] Wang Y, Kang Z, He Q. Adaptive topology optimization with independent error control for separated displacement and density fields. Computers & Structures 2014;135:50–61.

[8] Grote MJ, Kray M, Nahum U. Adaptive eigenspace method for inverse scattering problems in the frequency domain. Inverse Problems 2017;33(2):025006.

[9] Grote MJ, Nahum U. Adaptive eigenspace for multi-parameter inverse scattering problems. Computers & Mathematics with Applications 2019;77(12):3264–3280.

[10] De Buhan M, Darbas M. Numerical resolution of an electromagnetic inverse medium problem at fixed frequency. Computers & Mathematics with Applications 2017;74(12):3111–3128.

[11] Bendsøe MP. Optimal shape design as a material distribution problem. Structural optimization 1989;1(4):193–202.

[12] Wang F, Lazarov BS, Sigmund O. On projection methods, convergence and robust formulations in topology optimization. Structural and Multidisciplinary Optimization 2011;43(6):767–784.

[13] Hinze M, Pinnau R, Ulbrich M, Ulbrich S. Optimization with PDE constraints, vol. 23. Springer Science & Business Media; 2008.

[14] Guest JK, Asadpoure A, Ha SH. Eliminating beta-continuation from heaviside projection and density filter algorithms. Structural and Multidisciplinary Optimization 2011;44(4):443–453.

[15] Xu S, Cai Y, Cheng G. Volume preserving nonlinear density filter based on heaviside functions. Structural and Multidisciplinary Optimization 2010;41(4):495–505.

[16] Burger M, Stainko R. Phase-field relaxation of topology optimization with local stress constraints. SIAM Journal on Control and Optimization 2006;45(4):1447–1466.

[17] Strong D, Chan T. Edge-preserving and scale-dependent properties of total variation regularization. Inverse problems 2003;19(6):S165.

[18] Lazarov BS, Wang F. Maximum length scale in density based topology optimization. Computer Methods in Applied Mechanics and Engineering 2017;318:826–844.

[19] Constrained Nonlinear Optimization Algorithms - MATLAB & Simulink;. `https://www.mathworks.com/help/optim/ug/constrained-nonlinear-optimization-algorithms.html`.

[20] Svanberg K. The method of moving asymptotes—a new method for structural optimization. International journal for numerical methods in engineering 1987;24(2):359–373.

[21] Sigmund O. Morphology-based black and white filters for topology optimization. Structural and Multidisciplinary Optimization 2007;33(4-5):401–424.

[22] Zhou M, Lazarov BS, Wang F, Sigmund O. Minimum length scale in topology optimization by geometric constraints. Computer Methods in Applied Mechanics and Engineering 2015;293:266–282.

[23] Gaynor AT, Guest JK. Topology optimization considering overhang constraints: Eliminating sacrificial support material in additive manufacturing through design. Structural and Multidisciplinary Optimization 2016;54(5):1157–1172.

[24] Stolpe M, Svanberg K. An alternative interpolation scheme for minimum compliance topology optimization. Structural and Multidisciplinary Optimization 2001;22(2):116–124.